Spring 2019

Development of Acceptor-Integrated Crystalline Organic Materials

Brandon Yarbrough

DEVELOPMENT OF ACCEPTOR-INTEGRATED CRYSTALLINE ORGANIC MATERIALS

by

Brandon Yarbrough

Bachelor of Arts
Coker College, 2016

Submitted in Partial Fulfillment of the Requirements

For the Degree of Master of Science in

Chemistry

College of Arts and Sciences

University of South Carolina

2019

Accepted by:

Natalia B. Shustova, Director of Thesis

Aaron K. Vannucci, Reader

Cheryl L. Addy, Vice Provost and Dean of the Graduate School

ABSTRACT

We report the first example of fullerene-containing porous covalent-organic scaffold, which combines not only crystallinity and porosity, but also integrates the intrinsic properties of a redox-active buckyball, along with the ability to tune electronic properties. Thus, the presented studies not only demonstrate the possibility of merging the strong electron accepting properties of fullerene-based derivatives with the versatility of covalent-organic frameworks (COFs), but also begin the class of crystalline, entirely organic, donor-acceptor fullerene COFs through covalently modifying the channel walls. These studies could foreshadow new avenues for buckyball utilization for applications ranging from organic photovoltaics to molecular electronics.

TABLE OF CONTENTS

LIST OF FIGURES

CHAPTER 1

REDOX-ACTIVITY AND ELECTRONIC STRUCTURES OF WELL-DEFINED DONOR-ACCEPTOR FULLERETIC COVALENT-ORGANIC MATERIALS

The merging of fullerene and their derivatives with covalent-organic frameworks (COFs) presents potential avenues for the engineering of organic photovoltaics and molecular electronics due to their electron accepting properties and ultrafast electron/energy transfer in combination with crystalline, porous motifs that allow for the precise integration of these building blocks.[1-13] The arrangement of fullerene is crucial for efficient energy or charge transfer as it can influence the distance of exciton diffusion, π-π stacking, or Forster radius, and as a result, the formation of fullerene stacks can provide a platform for enhanced device performance.[14] The ability to combine the excellent electron accepting properties of fullerene with a framework with donating character could lead to significant enhances in conductivity, with up to a six order of magnitude increase in comparison to the COF itself, which could lead to the extension of a novel synthetic architecture into potential future applications. While electrically conductive COFs are few in number, they can be considered as an intriguing subclass of materials, especially with the scope of the insulating nature of most COFs.[15]

Herein, we demonstrated, for the first time, how the coordination a fullerene-based derivative, within an insulating porous organic scaffold could modify the electronic properties, resulting in changes in electronic properties, as well as maintenance of the redox activity of the precursors after incorporation. As fullerene-based derivatives are a

logical starting point for these studies due to their curvature, ability to accommodate multiple electrons, and widespread use in organic solar cell applications,[23–26] it is also intriguing to investigate how the well-known strong acceptor, (tetracyanoquinodimethane, TCNQ), will behave when integrated in the same COF. Although there are other studies in the literature of the inclusion of strong acceptors in COFs/MOFs leading to a conductivity enhancement,[27–29] this work is unique in the aspect of being the first account of TCNQ covalently bound in a COF, along with the corresponding conductivity studies. In addition to being the only report of increased conductivity through the coordination of strong acceptors (i.e. TCNQ and fullerene-based derivatives) within an insulating scaffold, the resulting acceptor-containing materials are the first members in the family of crystalline, entirely organic, donor-acceptor fullerene-based COFs, as other examples of covalently modifying the channel walls of donor/acceptor COFs have involved metal coordination in the COF itself or inclusion of the fullerene derivative as a guest.[30–33] Furthermore, the resulting acceptor-containing materials maintained porosity while providing a pathway for electrons, ultimately reinforcing semi-conducting behavior in generally insulating porous materials (for instance, covalent-organic or metal-organic frameworks (COFs/MOFs)). Our approach involves the fusion of both structural and spectroscopic analysis to investigate the proposed donor-acceptor alignment within the prepared framework.

To rationally construct and study a crystalline donor-acceptor redox-active organic framework, 1,3-cycloaddition, [2+2] cycloaddition, and Sonogashira coupling were employed (Figure 1.2).[34–36] The choice of the host for post-synthetic modification was determined by following criteria: (i) sufficient pore aperture to accommodate bulky

electron acceptors such as fullerenes (the fullerene diameter (7 Å), the length of TCNQ (8 Å)), (ii) contains functional groups promoting cycloaddition or coupling reactions, and (iii) maintains structural integrity after derivatization. The first two strategies (1,3- and [2+2]cycloaddition) were utilized to integrate strong electron acceptors (i.e., fullerene and TCNQ moieties), while the third strategy (Sonogashira coupling) was used to probe inclusion of fluorophore tags (vide infra).

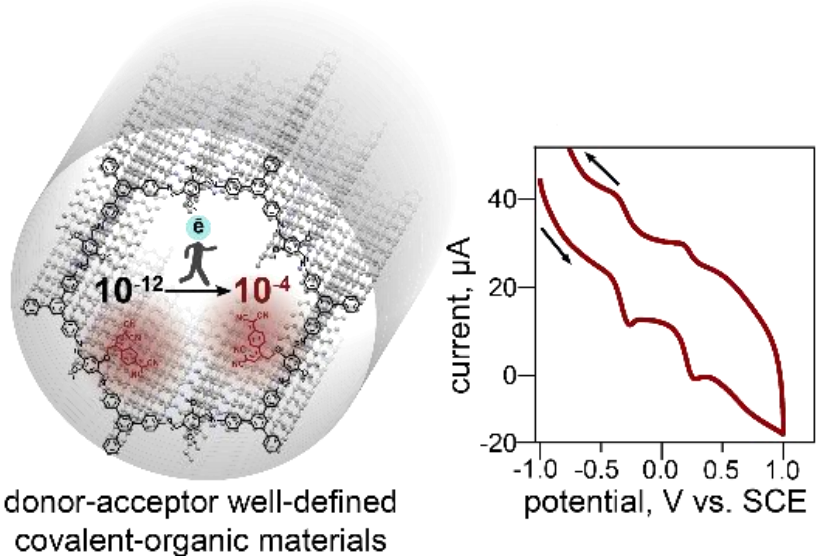

Figure 1.1. (*left*) A schematic representation of well-defined donor-acceptor redox-active porous materials. (*right*). The cyclic voltammetry curve of crystalline porous material, TCNQ[**1≡(34%)**], derivatized with TCNQ electron-accepting units highlights retention of redox-active properties. The measurements were carried out in a DMF solution containing 0.1 M tetrabutylammoniumhexafluorophosphate, TCNQ[**1≡(34%)**] (40 wt.%) and carbon black (60 wt.%), and 0.1 mL of Nafion using an glass solution reservoir equipped with saturated calomel reference, platinum wire counter, and gold working electrodes.

For integration of electron-acceptors, the COF, **1≡(x%)** (where *x* = [BPTA]/([BPTA]+[DMTA]) × 100%; Figure 1.2) have been prepared from 2,5-bis(2-propynyloxy) terephthalaldehyde (BPTA), 2,5-dimethoxyterephthalaldehyde (DMTA),

and tri-(4-aminophenyl)benzene (TAPB, see Supplementary Information for synthetic details).[35] This framework satisfies the criteria listed above as it: (i) has open 30 Å-channels, (ii) provides the ability to maintain structural integrity over a large pH range, and (iii) contains alkyne groups for postsynthetic derivatization.

The methodology for development of donor-acceptor materials includes two-steps: (i) several-day pre-soaking of, for instance, fullerene derivatives inside the large (~30 Å) COF channels promoting acceptor diffusion and (ii) addition of the reagents required for a 1,3-cycloaddition reaction (Figure 1.2) followed by heating (*N*,*N*-diisopropylethylamine/CuI/toluene/H_2O, 70 °C, 3 days). Synthesis of the fullerene derivative, 2-(azidoethyl)-(ethyl)-3'H-cyclopropa-[1,2](C_{60})[5,6]fullerene-3',3'-dicarboxylate (NEM-C_{60}, Figure 1.2), suitable for the cycloaddition reaction and accessible on a g-scale without use of the labor-demanding high pressure liquid chromatography (HPLC) was performed using a 3-step procedure.[37]

Prior investigations with bulky and relatively expensive fullerene-containing precursors, we systematically studied the reaction conditions applicable for 1,3-cycloaddition starting with less bulky and more affordable azide-based derivatives such as 2-azidoethanol and 2-azidoethyl ethyl malonate. Then, the reaction conditions developed for cycloaddition of the small azide-based derivatives (*N*,*N*-diisopropylethylamine/CuI/THF/H_2O, 70 °C, 3 d) were applied for integration of 2-azidoethyl ethyl malonate (NEM) inside the COF (**1≡(34%)**, see the Supplementary Information). Spectroscopic techniques including FTIR and solid-state ^{13}C cross-polarization magic-angle spinning (CP-MAS) NMR spectroscopies, as well as a method based on the integration of the fluorophore tag (vide infra), were used to monitor reaction

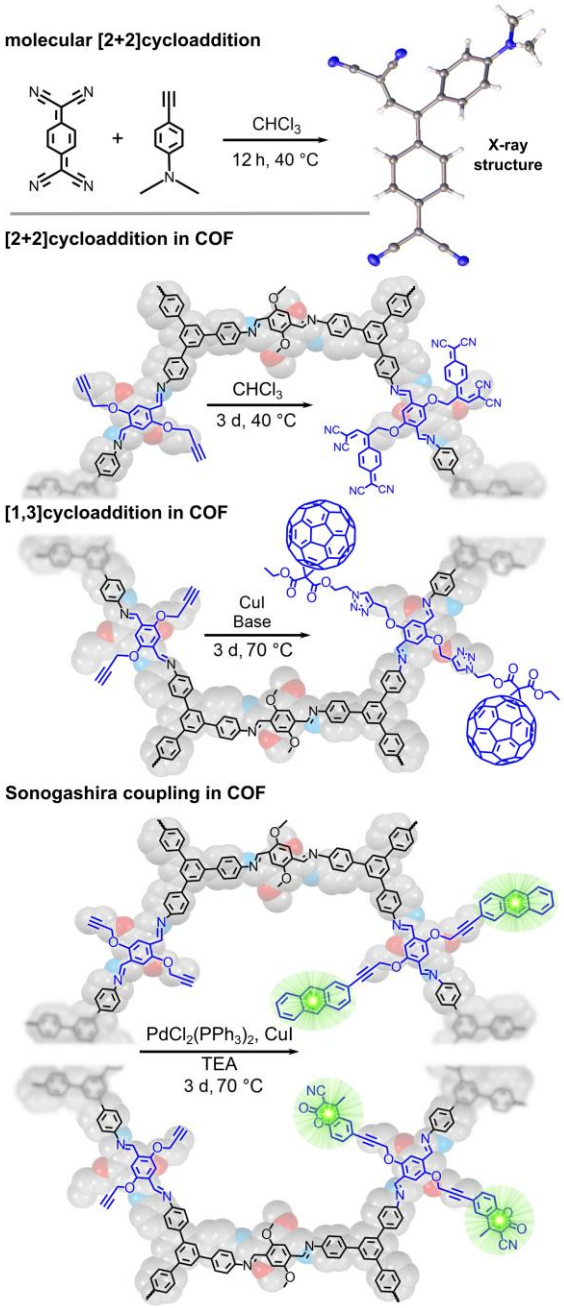

Figure 1.2. (*top*) Reaction conditions involving TNCQ moieties in a molecular [2+2]cycloaddition, as well as the single crystal structure. (*middle*) Reaction conditions used for [2+2]cycloaddition in the COF for TCNQ integration and 1,3- cycloaddition for NEM-C_{60}[**1≡(34%)**]formation. (*bottom*) Reaction conditions used for Sonogashira coupling in the COF for fluorescent tag integration.

progress in the solid state. Control experiments, in which the COF was subjected to the same reaction conditions, but without the addition of the azide-containing precursor were also carried out. In the case of FTIR spectroscopic studies, we monitored the disappearance of 2120 cm^{-1} (C≡C) and 3300 cm^{-1} (C≡C–H) bands (Figures 1.3 and 1.4), while in the control experiment both bands were preserved (Figure 1.10).

Once the cycloaddition conditions had been developed on the example of relatively small electron-acceptors, we ultimately focused on the integration of NEM-C_{60} (Figure 1.2). Based on the combined spectroscopic data, gas-sorption analysis, and fluorophore tag experiments, incorporation of the azide building block resulted in the successful formation of NEM-C_{60}[**1≡(34%)**] (see the Supplementary Information for more details). In particular, ^{13}C CP-MAS spectroscopic studies demonstrated disappearance of the C≡C band in contrast to the control experiment (without presence of the azide precursor under the same reaction conditions). Moreover, FTIR spectroscopic studies confirmed disappearance of C≡C resonance as well as appearance of carbonyl stretches (2100 cm^{-1}) of the diethyl malonate moiety (Figure 1.3). The substantial decrease of Brunauer-Emmett-Teller (BET) surface area from 1253 m^2g^{-1} (**1≡(34%)**) (Figure 1.20) to 229 m^2g^{-1} (NEM-C_{60}[**1≡(34%)**]) (Figure 1.21) also supports incorporation of bulky fullerene derivatives inside the porous scaffold. Although the surface area for a covalently linked fullerene was slightly higher (393 m^2/g) in a metallo-porphyrin COF,[30] we report the highest surface area determined for a purely organic COF with covalently bound fullerene acceptors to date.

The steady-state and time-resolved spectroscopic studies (described below) have also confirmed integration of electron-accepting units inside the electron-donating host (vide

infra). The synthesized material also maintained crystallinity as evident through wide-angle X-ray scattering (WAXS) (Figure 1.13) even after multiple cycles of the 1,3-cycloaddition reaction to maximize fullerene content, resulting in the first example of a crystalline, porous, and fully organic covalently-linked fullerene-based COF.

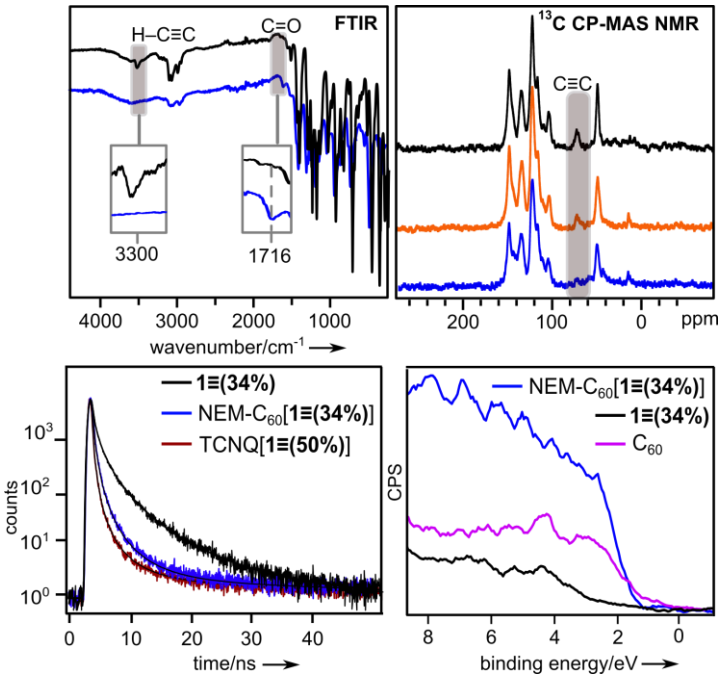

Figure 1.3. (*top left*) FTIR spectra of **1≡ (34%)** (black) and NEM-C_{60}[**1≡ (34%)**] (blue). Grey areas show H–C≡C and C≡C stretches, present in **1≡ (34%)** and absent in NEM-C_{60}[**1≡ (34%)**]. (*top right*) ^{13}C CP-MAS NMR spectra of **1≡ (34%)** (black), a control experiment with **1≡(34%)** (orange), and NEM-C_{60}[**1≡ (34%)**] (blue). (*bottom left*) Fluorescent decays of **1≡(34%)** (black), NEM-C_{60}[**1≡ (34%)**] (blue), and TCNQ[**1≡ (50%)**] (red). (*bottom right*) XPS data for the valence band region for **1≡(34%)** (black), C_{60} (pink), and NEM-C_6 [**1≡ (34%)**] (blue).

While fullerene C_{60} possesses a unique spherical cage allowing to stabilize up to six electrons, the LUMO of C_{60} is comparable with another well-known electron acceptor, TCNQ (-4.23 eV vs -4.50 eV (C_{60})).[38,39] In addition, TCNQ derivatives usually do not

require the labor-intensive HPLC procedure for their isolation in contrast to fullerene compounds with a large number of the active centers and possible isomers.[10] Thus, as a second type of donor-acceptor materials, we synthesized TCNQ-integrated COFs.

To develop suitable reaction conditions to perform a [2+2] cycloaddition reaction, we started with the molecular building blocks of TCNQ and 4-ethynyl-N,N-dimethylaniline (Figure 1.2) in order to monitor the reaction progress using "conventional" solution NMR spectroscopy. Formation of the desired product, 2-(4-(4,4-dicyano-2-(4-(dimethylamino)phenyl)butylidene)cyclohexa-2,5-dien-1-ylidene)malononitrile, was confirmed by NMR spectroscopy (Figures 1.17) and single-crystal X-ray crystallography (Figure 1.2 and 1.16). As a next step, the developed conditions were applied toward the reaction of TCNQ with the COF ((**1≡(34%)**). For comprehensive characterization of prepared TCNQ[**1≡(x%)**], we used the same set of techniques as in the case of NEM-C_{60}[**1≡(34%)**]. For instance, we observed the disappearance of 2120 cm^{-1} (C≡C) and 3300 cm^{-1} (C≡C–H) bands in the FTIR spectrum, while appearance of the nitrile stretch at 2100 cm^{-1} (C≡N) persisted after the reaction, even after a 24-hour Soxhlet washing procedure, highlighting the presence of TCNQ covalently bound in the COF (Figure 1.7). Due to smaller size of TCNQ versus relatively bulky NEM-C_{60}, the measured BET surface area even after TCNQ integration and was found to be 812 m^2g^{-1} (Figure 1.22). Thus, the determined value is the highest one for a TCNQ-covalently-linked COF to date in contrast to the previous reports mainly focused on infiltration of TCNQ molecules as guests.[15]

In addition to spectroscopic methods and gas sorption analysis, fluorescent labeling was utilized to address the question relative residual unreacted alkynes sites.

Two chromophores, 6-bromo-3-cyano-4-methylcoumarin and 2-bromoanthracene, were selected to perform Sonogashira coupling inside the functionalized COF (Figure 1.2). As a control experiment, we integrated the coumarin and anthracene moieties inside **1≡(50%)**. We observed a strong fluorescent signal for both (anthracene[**1≡(50%)**] and 4-methyl-2-oxo-2*H*-chromene-3-carbonitrile[**1≡(50%)**] (Figures 1.26–1.29). We applied the developed strategy towards detection of residual alkyne moities in TCNQ[**1≡(50%)**]. As a result, there was no emission detected for TCNQ[**1≡(50%)**] after the treatment with both fluorescent tags (Figure 1.28–1.29). These findings are in line with the spectroscopic evidences and confirm the lack of unreacted alkyne sites concluding reaction completion.

In order to understand the electronic structures and photophysical properties of the donor-acceptor redox-active materials, comprehensive analysis including diffuse reflectance (DR), steady-state and time-resolved photoluminescence (PL), and X-ray photoelectron (XPS) spectroscopies, cyclic voltammetry (CV), and conductivity measurements were employed.

Integration of either TCNQ moieties or fullerene-based electron-acceptors inside the COF was accompanied a drastic color change from pale yellow to dark red (Figure 1.4). DR spectroscopic studies confirm that acceptor integration resulted in the appearance on an additional absorption band leading to the bathochromic shift of the absorption profile in comparison with both the parent COF, fullerene, and TCNQ, which is typically associated with charge transfer.[27,40] To further study the observed behavior of both fullerene and TCNQ-modified COFs, we have utilized time-resolved PL spectroscopy. With the assumption that the PL decay rate consists of radiative, nonradiative, and CT components, analysis should reveal shortening of PL lifetimes of the host owing to

integration of the strong acceptor moieties (i.e., fullerene-based derivative or TCNQ).[41] The amplitude-averaged lifetime estimated by fitting the time-resolved PL decay curves were 474 ps (**1≡(34%)** while NEM-C_{60}[**1≡(34%)**] and TCNQ[**1≡(50%)**] exhibited much shorter lifetimes of 32 ps and 103 ps, respectively. This is indicative of the potential for CT in the system (Figure 1.3). Similar behavior was previously reported in the literature for fullerene inclusion as host molecules.[32] In addition, the emission response of the COF itself was quenched when either TCNQ or NEM-C_{60} were covalently bound to the COF walls (Figure 1.31).

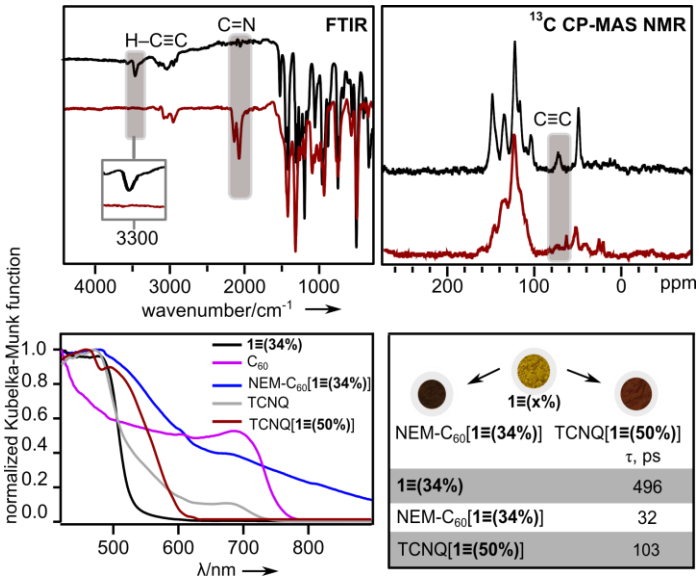

Figure 1.4. (*top left*) FTIR spectra of **1≡(34%)** (black) and TCNQ[**1≡(50%)**] (red). Grey areas show H–C≡C and C≡C stretches, present in **1≡(34%)** and absent in TCNQ[**1≡ (50%)**]. (*top right*) ^{13}C CP-MAS NMR spectra of **1≡(34%)** (black) and TCNQ[**1≡ (50%)**] (red). (*bottom left*) Normalized diffuse reflectance spectra of **1≡(34%)** (black), C_{60} (pink), NEM-C_{60}[**1≡ (34%)**] (blue), TCNQ (grey), and TCNQ[**1≡(50%)**] (red). (*bottom right*) Photographs of **1≡(x%)**, NEM-C_{60}[**1≡ (34%)**], and TCNQ[**1≡(50%)**]. The table shows the amplitude-weighted average lifetimes for **1≡(34%)**, NEM-C_{60}[**1≡ (34%)**], and TCNQ[**1≡(50%)**].

XPS was used to probe the electronic structure of the fullerene-based COFs by monitoring the density of states (DOS) near the Fermi level (E_F, binding energy = 0 eV) as a fast and nondestructive pre-screening technique. For fullerene itself, the valence band spectrum exhibits behavior associated with insulating materials, giving there is near zero intensity within 3 eV of the Fermi level. The spectrum of **1≡(34%)** itself also shows zero intensity at 2 eV. In contrast, the XPS valence band spectrum for NEM-C_{60}[**1≡(34%)**] showed much higher intensity within 2 eV of E_F. This indicates a greater DOS near E_F, which could be associated with a higher electrical conductivity. The conductivity increases with the inclusion of strong acceptors inside the donating scaffold is in line with literature reports.[28]

To test if the amount of the electron-accepting moieties inside the COF can affect the electronic properties of the prepared materials, we prepared a series of donor-acceptor COFs integrating a different number of TCNQ fragments such as TCNQ[**1≡(34%)**] and TCNQ[**1≡(100%)**]. The bulk conductivity measurements demonstrate an order of magnitude difference for TCNQ[**1≡(34%)**] (1.7×10^{-7} S/cm) versus TCNQ[**1≡(100%)**] (2.1×10^{-6} S/cm), respectively, which is a six order of magnitude increase in comparison to the COF itself (2.3×10^{-12} S/cm). The conductivity of NEM-C_{60}[**1≡(34%)**] was measured to be 1.97×10^{-6} S/cm. The effect of iodine doping has been also studied which led to increase of conductivities in the range of two to four orders of magnitude with values of 5.06×10^{-8} S/cm, 1.08×10^{-5} S/cm, and 1.41×10^{-4} for the COF, TCNQ[**1≡(50%)**], and TCNQ[**1≡(100%)**], respectively. The conductivity of NEM-C_{60}[**1≡(34%)**] increased to 3.63×10^{-5} S/cm when doped with iodine. The values obtained herein are among some of the highest values reported in COFs to date.[13–19] In

addition, these conductivity studies are among the first reports for the TCNQ-integrated COFs.

To test the redox properties of the prepared NEM-C_{60}[**1≡(34%)**] and TCNQ[**1≡(34%)**], significant modifications of the commonly used electrochemical setup were employed[42] as cyclic voltammetry studies of COFs are still relatively rare. The redox-active COFs (40 wt%) were combined with carbon black and Nafion, and the obtained slurry was pipetted onto the tip of the electrode and dried under high vacuum. Cyclic voltammetry of TCNQ itself (1.0×10^{-4} M) was performed in a 0.1 M solution of tetrabutylammonium hexafluorophosphate in acetonitrile to afford one reversible reduction at E_p = –0.5 V and one oxidation at 0.1 V vs. SCE (Figure 1.22). Comparison of the acquired CV data for TCNQ[**1≡(34%)**] to TCNQ itself, shows that the both potentials of TCNQ[**1≡(34%)**] are less negative at E_p = –0.3 V and 0.2 V vs. SCE (Figure 1.1), which can confirm the stronger electron accepting properties of the prepared material. Moreover, inclusion of TCNQ in a COF affects the redox potential, which enables this compound to be electrochemically sensed.[43] In comparison with fullerene itself which exhibits four reversible reductions at E_p = –0.3 V, –0.7 V, –1.4 V, and –1.9 V in DMF vs. SCE, the NEM-C_{60} shows similar redox features at E_p = –0.9 V and –1.8 V (Figures 1.21 and 1.23). The reduction waves are more negative than that of pristine C_{60}, which is a well-known consequence of the saturation of a double bond on the fullerene sphere.[44] The redox potentials of NEM-C_{60} (E_p = –0.9 V and –1.8 V) and NEM-C_{60}[**1≡(34%)**] (E_p = -1.2 V and -2.1 V vs. SCE) are also similar, with a slight shift in potential (Figures 1.23 and 1.24) supporting integration of NEM-C_{60} and reinforcement of the redox active nature within the COF. Such electrochemical behavior (i.e., presence of

two waves in the cyclic voltammogram) is comparable with fullerene-based dimers in the literature,[44] with a reduced symmetry comparable to NEM-C_{60}. While CVs with integrated acceptors have been measured for other systems such as molecular rectangles,[43] these are the first studies, to the best of our knowledge, that demonstrate redox active behavior of TCNQ- and fullerene-integrated COFs.

The preceding results highlight the first examples of acceptor-based (purely organic) covalently bound, crystalline and porous scaffolds that not only exhibit increases in conductivity by 8 orders of magnitude, but also retain the redox properties of the strong acceptor precursor after integration. For the first time, [2+2]cycloaddition and Sonagashira couplings were employed with a COF, highlighting the potential for COFs in a wide range of reactions. The use of spectroscopy and conductivity measurements sheds light on the improved electronic structure of an insulating framework prior to integration and are among some of the most conductive COFs to date. Overall, this work demonstrates the potential to tune the electronics of porous materials through the inclusion of strong organic acceptors, while maintaining structural integrity and porosity; and this combination could open a new avenue for the rational design of electroactive and conductive multidimensional crystalline porous materials.

EXPERIMENTAL SECTION

Materials. 2-bromoethanol (97%, BeanTown Chemical), sodium azide (99%, Oakwood Chemical), ethyl malonyl chloride (95%, Oakwood Chemical), DBU (1,8-diazabicyclo[5.4.0]undec-7-ene) (98%, Acros Organics), carbon tetrabromide (98%, Acros Organics), C_{60} fullerene (>99.5%, Solaris Chemicals), 7,7,8,8-tetracyanoquinodimethane (>98%, TCI Chemicals), copper(I) iodide (reagent grade,

Millipore Sigma), *N*,*N*-diisopropylethylamine (>98%, Millipore Sigma), bis(triphenylphosphine)palladium(II) dichloride (95%, Oxchem), 1,3,5-tribromobenzene (98%, Sigma-Aldrich), aliquat 336 (reagent grade, Beantown chemical), bromine (reagent grade, Sigma-Aldrich), 1,4-dimethoxybenzene (reagent grade, Oakwood Chemical), *n*-butyllithium (reagent grade, Sigma-Aldrich), boron tribromide (reagent grade, Sigma-Aldrich), propargyl bromide (80% weight in toluene, reagent grade, Oakwood Chemical), potassium carbonate (99.8%, Mallinckrodt), 4-aminophenyl boronic ester (reagent grade, Oakwood Chemical), acetic acid (ACS grade, Fisher Scientific), 1-butanol (reagent grade, Oakwood Chemical), *o*-dichlorobenzene (ACS grade, Alfa Aesar), 1,4-dioxane (99+%, Alfa Aesar), anhydrous magnesium sulfate (reagent grade, J.T. Baker® Chemicals), *N*,*N*-dimethylformamide (ACS grade, BDH), dichloromethane (ACS grade, Macron), chloroform (ACS grade, Macron), hydrochloric acid (ACS grade, EMD Chemicals), 2-bromoanthracene (reagent grade, Oakwood Chemical), 6-bromo-3-cyano-4-methylcoumarin (97%, Sigma-Aldrich), triethylamine (99.5%, Sigma-Aldrich), nitric acid (ACS grade, Fisher Scientific), methanol (HPLC grade, Fisher Scientific), toluene (HPLC grade, Fisher Scientific), acetonitrile (ACS grade, Fisher Scientific), tetrahydrofuran (ACS grade, EMD Chemicals), iodine (ACS grade, Fisher Scientific), ethyl acetate (HPLC grade, Fisher Scientific), silica gel (Macron), sodium chloride (ACS grade, Fisher Scientific), chloroform-*d* (Cambridge Isotope Laboratories, Inc.), and DMSO-d_6 (Cambridge Isotope Laboratories, Inc.) were used as received.

The COF-based linkers, 2,5-dimethoxyterephthalaldehyde (DMTA), 1,3,5-tri-(4-aminophenyl)benzene (TAPB), and 2,5-bis(2-propynyloxy) terephthalaldehyde (BPTA),

were synthesized based on modified literature procedures.[45-46] The COFs, **1≡(x%)** (where x = [BPTA]/([BPTA] + [DMTA]) × 100%), were also synthesized based on modified literature procedures.[47-48]

Synthesis of 2-azidoethanol ($C_2H_5ON_3$).

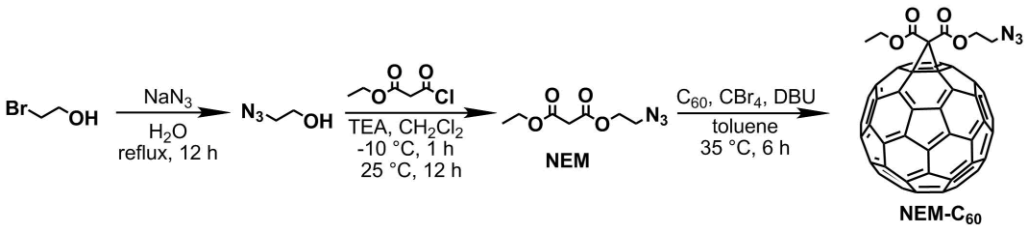

Preparation of 2-azidoethanol was performed based on a modified literature procedure.[49] In a 100-mL Schlenk flask under a nitrogen atmosphere, 2-bromoethanol (1.0 g, 8.0 mmol) was added to NaN_3 (0.78 g, 12 mmol) and then the reaction mixture was heated at reflux in water (7.2 mL) for 12 hours. Once cooled to room temperature, NaCl (1.0 g, 17 mmol) was added to the reaction mixture. The desired compound was extracted from the aqueous layer using dichloromethane (3 × 25 mL) and the solvent was removed under reduced pressure, resulting in a yellow oil. A yield of 80% was obtained. ^{1}H NMR (DMSO-d_6, 300 MHz): δ = 5.00 (1H, t, J = 5.04), 3.57 (2H, q, J = 5.04), 3.26 (2H, t, J = 5.04) ppm (Figure 1.5). ^{13}C NMR (DMSO-d_6, 101 MHz): δ = 63.51 and 53.42 ppm (Figure 1.5). FTIR (neat, cm^{-1}): 3353, 2936, 2093, 1635, 1442, 1347, 1284, 1061, 977, 878, and 829 (Figure 1.7).

Synthesis of 2-azidoethyl ethyl malonate ($C_7H_{11}O_4N_3$, NEM).

Preparation of NEM was performed based on a modified literature procedure.[49] A 50-mL Schlenk flask was charged with 2-azidoethanol (0.35 g, 4.0 mmol) and anhydrous dichloromethane (20 mL). Once the solution was cooled to –10 °C using a dry ice/ethylene glycol bath, anhydrous triethylamine (0.71 mL, 5.0 mmol) and ethyl malonyl

chloride (0.52 mL, 4.0 mmol) were added slowly to the mixture. The solution was kept at –10 °C for one hour, then slowly warmed to room temperature, and stirred overnight. The resulting solution was quenched with water (20 mL) and extracted with dichloromethane (3 × 25 mL). The combined organic layers were washed with water (3 × 25 mL) and the solvent was removed under reduced pressure resulting in a yellow oil. A yield of 93% was obtained. ^{1}H NMR ($CDCl_3$, 300 MHz): δ = 4.32 (2H, t, J = 5.04), 4.22 (2H, q, J = 7.14), 3.51 (2H, t, J = 5.04), 3.43 (2H, s), 1.29 (3H, t, J = 7.14) ppm (Figure 1.6). ^{13}C NMR (DMSO-d_6, 101 MHz): δ = 166.27, 64.08, 61.83, 48.92, 41.73, 14.06 ppm (Figure 1.6). FTIR (neat, cm^{-1}): 2985, 2105, 1741, 1445, 1369, 1328, 1266, 1144, 1031, 959, 847, and 680 (Figure 1.8). HRMS (ESI, m/z) calculated for $[NEM+H]^+$ 202.0828, found 202.0831.

Development of the Synthetic Conditions for 1,3-Cycloaddition Reactions.

For investigation of reaction conditions necessary to perform a 1,3-cycloaddition using NEM-C_{60} with **1≡(34%)**, we devised a stepwise approach starting with azide-containing molecules. We initially chose less bulky and more affordable units such as 2-azidoethanol and NEM for development of synthetic methodologies before pursuing the reaction between NEM-C_{60} and **1≡(34%)**.

*Synthesis of 2-azidoethanol**[1≡(34%)]**.*

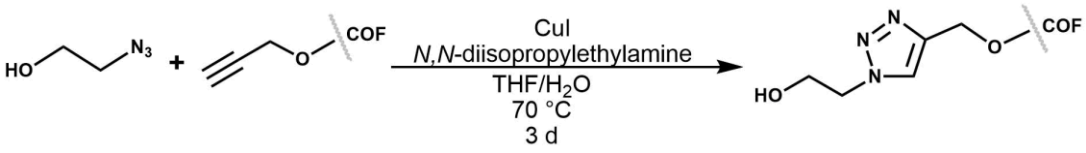

In a 25-mL Schlenk tube, 2-azidoethanol (4.4 mg, 51 µmol), **1≡(34%)** (15 mg), *N*,*N*-diisopropylethylamine (75 µL of a 1.0 M THF solution), and CuI (1.5 mg, 7.5 µmol) in a mixture of THF/water (2.0 mL/0.75 mL) were added. The reaction mixture was

degassed through three freeze-pump-thaw cycles and the mixture was heated at 70 °C for three days. Upon cooling to room temperature, the solid was collected via vacuum filtration, washed thoroughly with THF and acetonitrile, and dried under reduced pressure to give a brown solid in quantitative yield. FTIR (neat, cm^{-1}): 2926, 1591, 1505, 1465, 1412, 1293, 1209, 1034, 823, and 697. The FTIR data highlight disappearance of the alkyne bands, ν(C≡C), at 2120 cm^{-1} and ν(H–C≡C) at 3300 cm^{-1} and appearance of the alcohol band ν(OH) at ~2900 cm^{-1} in the spectrum, which is indicative of reaction completion (Figure 1.10).

*Synthesis of NEM**[1≡(34%)]**.*

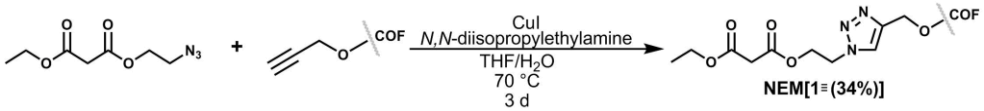

In a 25-mL Schlenk tube, COF **1≡(34%)** (15 mg), NEM (6.8 mg, 51 μmol), *N*,*N*-diisopropylethylamine (75 μL of a 1.0 M THF solution), CuI (1.5 mg, 7.5 μmol), and THF/water (2.0 mL/0.75 mL) were added. The reaction mixture was degassed through three freeze-pump-thaw cycles and the mixture was heated at 70 °C for three days. Upon cooling to room temperature, the precipitate was collected via vacuum filtration, washed with THF and acetonitrile, and dried under reduced pressure to give a brown solid in quantitative yield. FTIR (neat, cm^{-1}): 2962, 1737, 1594, 1505, 1412, 1284, 1210, 1035, 828, and 697. The FTIR data highlight disappearance of the alkyne bands, ν(C≡C), at 2120 cm^{-1} and ν(H–C≡C) at 3300 cm^{-1} and appearance of the carbonyl band ν(–C=O) at ~1700 cm^{-1}, which is indicative of reaction completion. The control experiment was also performed and discussed below.

*Control Experiment Involving **1≡(34%)**.*

As a control experiment, we treated **1≡(34%)** under the same reaction conditions developed for the 1,3-cycloaddition reactions (such as in the synthesis of NEM[**1≡(34%)**]), but without presence of the azide-containing precursor. As expected, we observed preservation of both 2120 cm^{-1}, ν(C≡C), and 3300 cm^{-1}, ν(H–C≡C), bands in the FTIR spectrum showing that the alkyne moieties within the COF pores were not affected (Figure 1.15).

In a 25-mL Schlenk tube, CuI (1.5 mg, 7.5 μmol) and **1≡(34%)** (15 mg) were added to a mixture of THF/H_2O (2.0 mL/0.75 mL). To the prepared reaction mixture, *N,N*-diisopropylethylamine (75 μL of a 1.0 M THF solution) was added. The reaction mixutre was degassed through three freeze-pump-thaw cycles and the mixture was stirred at 70 °C for three days. Upon cooling to room temperature, the precipitate was collected, washed with THF and acetonitrile, and dried under vacuum overnight to give a brown solid in quantitative yield. FTIR (neat, cm^{-1}): 3300, 2120, 1673, 1596, 1510, 1458, 1394, 1284, 1210, 1185, 1029, 879, 824, 732, and 695 (Figure 1.15).

*Synthesis of NEM-C_{60}**[1≡(34%)]**.*

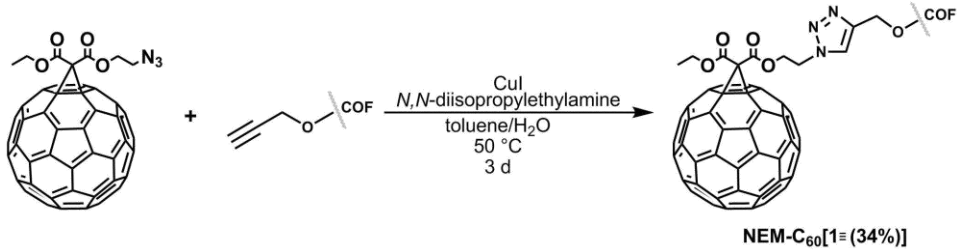

Initially, we prepared (2-azidoethyl)-(ethyl)-3'H-cyclopropa-[1,2](C_{60})[5,6]fullerene-3',3'-dicarboxylate (NEM-C_{60}) according to a literature procedure.[49] In the absence of light, a 100-mL Schlenk flask was charged with C_{60} (50

mg, 69 μmol) and anhydrous toluene (50 mL). Once the C_{60} was fully dissolved, NEM (9.7 mg, 69 μmol), carbon tetrabromide (110 mg, 0.34 mmol), and 1,8-diazabicyclo[5.4.0]undec-7-ene (DBU) (21 mg, 0.14 mmol) were added to the solution. The solution was heated at 35 °C for six hours. The crude product was purified via gradient column chromatography (SiO_2, toluene → 1:1 toluene:dichloromethane) to afford the product with 51% yield. FTIR (neat, cm^{-1}): 2921, 2097, 1742, 1430, 1259, 1015, 795, and 703 (Figure 1.9). HRMS (ESI, m/z) calculated for $[NEM\text{-}C_{60}]^-$ 919.0593, found 919.0595. Cyclic voltammetry was used to study the redox potential of NEM-C_{60} in comparison with C_{60} itself (Figures 1.22 and 1.24, see the Physical Measurements section for more details). As a next step, isolated NEM-C_{60} was used for integration inside the COF. In order to avoid exposure to light during the reaction, a 25-mL Schlenk tube was wrapped with foil, and NEM-C_{60} (2.0 mL of a 15 μM toluene solution) was added to **1≡(34%)** (15 mg). The COF was then allowed to soak in the NEM-C_{60} solution for one day. As the next step, *N*,*N*-diisopropylethylamine (75 μL of a 1.0 M THF solution), CuI (0.5 mg, 2.5 μmol), and water (0.75 mL) were added to the reaction mixture. The reaction mixture was degassed through three freeze-pump-thaw cycles, wrapped with aluminum foil to prevent exposure to light, and then heated at 50 °C for three days. Upon cooling to room temperature, the precipitate was collected via vacuum filtration and washed thoroughly with THF and acetonitrile. In order to maximize fullerene content, the material was subjected to multiple cycles of soaking and the 1,3 cycloaddition. The collected precipitates were re-added to a solution of NEM-C_{60} (2.0 mL of a 15 μM toluene solution) in a foil-wrapped 25-mL Schlenk tube, and soaked in this solution for one day. The same reaction conditions (*N*,*N*-

diisopropylethylamine/CuI/THF/H_2O, 70 °C, 3 days) were repeated two additional times, until the reaction solution retained color, indicating complete incorporation of NEM-C_{60}. Lastly, upon cooling to room temperature, the solid was collected via vacuum filtration, washed with THF and acetonitrile, and dried under reduced pressure to give a brown solid in quantitative yield. FTIR (neat, cm^{-1}): 2921, 1742, 1683, 1591, 1504, 1409, 1287, 1209, 1037, 879, 827, and 732 (Figure 1.3). The FTIR data highlight disappearance of the alkyne bands, ν(C≡C), at 2120 cm^{-1} and ν(H–C≡C) at 3300 cm^{-1} in the FTIR spectra, which is indicative of reaction completion (Figure 1.3). In addition, presence of the characteristic carbonyl band, ν(-C=O), at ~1716 cm^{-1} from NEM-C_{60} in the FTIR spectrum of NEM-C_{60}[**1≡(34%)**] also supports reaction completion. The ^{13}C CP-MAS NMR spectroscopy was used as an additional technique to monitor reaction progress, since the alkyne (C≡C) is the reactive species, and is observed in the ^{13}C CP-MAS NMR spectrum for **1≡(34%)** (see Figure 1.3). This spectrum highlights disappearance of the alkyne (C≡C) resonance at 80 ppm, indicative of completion of the 1,3-cycloaddition reaction. In addition, the appearance of resonances at ~15 and 40 ppm may be attributed to the ethyl group of NEM-C_{60} (see ^{13}C NMR spectrum of NEM (Figure 1.6), further indicating reaction completion. In addition, WAXS data demonstrate crystallinity preservation of the modified framework indicating that structural integrity was maintained after undergoing multiple 1,3-cycloaddition reactions (Figure 1.13). Fitting the N_2 adsorption isotherm to the Brunauer-Emmett-Teller (BET) equation resulted in surface area of 229 m^2/g (Figure 1.21).

To further study the reaction between NEM-C_{60} and the COF, we employed diffuse reflectance (DR), steady-state and time-resolved photoluminescence (PL), and X-

ray photoelectron (XPS) spectroscopies, as well as conductivity measurements. Integration of electron-accepting units inside the COF resulted in a significant color change from yellow to brown. A DR spectroscopic analysis revealed that fullerene integration resulted in appearance of an additional absorption band (Figure 1.3), which can be attributed to charge transfer between COF and fullerene moieties. The analysis of time-resolved PL decay curves revealed an amplitude-averaged lifetime of 32 ps for NEM-C_{60}[**1≡(34%)**] in comparison with 496 ps for the COF itself (Figure 1.3). In addition, the presence of electron acceptor, such as NEM-C_{60} in the COF structure, resulted in complete PL quenching (Figure 1.32).

Development of the Synthetic Conditions for [2+2] Cycloaddition Reactions.

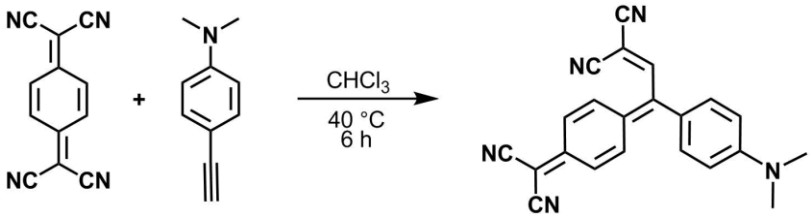

To demonstrate the ability of TCNQ to participate in [2+2] cycloaddition reactions with alkynes in the COF structure, the reaction was initially performed with molecular species in solution according to a modified literature procedure.[50] In a 50-mL Schlenk flask, 7,7,8,8-tetracyanoquinodimethane (70 mg, 0.34 mmol) and 4-ethynyl-*N*,*N*-dimethylaniline (50 mg, 0.34 mmol) were added to chloroform (20 mL). The resulting solution was heated at 40 °C for six hours. Once the solvent was removed under reduced pressure, the crude product was purified via column chromatography (SiO_2, dichloromethane) to afford the product with 51% yield. ^{1}H NMR spectrum (CD_2Cl_2, 300 MHz): δ = 8.18 (1H, s), 7.30 (4H, s), 7.15 (2H, d, J = 9.0), 6.78 (2H, d, J = 9.0), and 3.15 (6H, s) ppm (Figure 1.17). ^{13}C NMR spectrum (CD_2Cl_2, 101 MHz): δ = 156.63, 152.95,

152.89, 146.45, 135.74, 134.22, 126.39, 122.72, 114.08, 113.78, 112.31, 110.53, 92.58, 76.46, and 40.17 ppm (Figure 1.17). HRMS (ESI, m/z) calculated for $C_{22}H_{15}N_5$ $[M+H]^+$ 350.1406, found 350.1408. The product was recrystallized from a saturated benzene solution. Single-crystal X-ray data are shown in Table S1 and Figure 1.16.

*Synthesis of TCNQ**[1≡(x%)]**.*

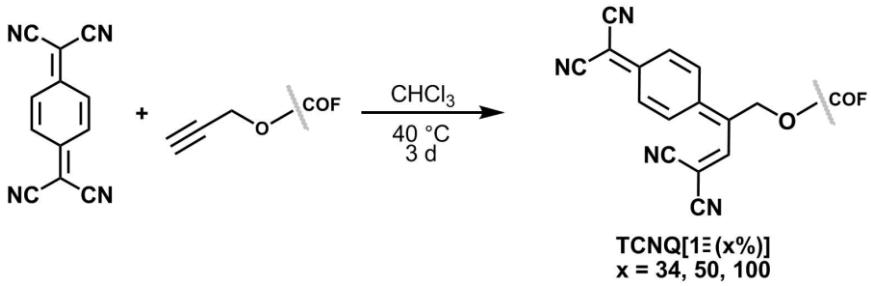

In a 25-mL Schlenk tube, COF **1≡(x%)** (15 mg) (where *x* = 34, 50, or 100), 7,7,8,8-tetracyanoquinodimethane (varying amounts based on alkyne percent in the pores:10 mg, 49 µmol for **1≡(34%)**; 15 mg, 75 µmol for **1≡(50%)**; 30 mg, 150 µmol for **1≡(100%)**), and chloroform (2.0 mL) were added. The flask was degassed through three freeze-pump-thaw cycles and the mixture was heated at 40 °C for three days. Upon cooling to room temperature, the solid was collected via vacuum filtration, washed with chloroform and acetonitrile, and dried under reduced pressure to give a brown solid in quantitative yield. FTIR (neat, cm^{-1}): 2962, 2104, 1737, 1594, 1505, 1412, 1284, 1210, 1035, 828, and 697. The FTIR data demonstrates disappearance of the alkyne bands, ν(C≡C), at 2120 cm^{-1} and ν(H–C≡C) at 3300 cm^{-1} and the appearance of the nitrile band, ν(C≡N), at 2100 cm^{-1}, which is indicative to reaction completion. Notably, preservation of bands corresponding to the TCNQ moiety after an extensive several-day washing procedure also supports successful reaction completion. The ^{13}C CP-MAS NMR

spectroscopy was used as an additional technique to monitor reaction progress. In all reactions (except the control experiment) the alkyne resonances, ν(C≡C), are present in the ^{13}C CP-MAS NMR spectra for every **1≡(x%)** and absent in the spectra after reaction completion (Figure 1.4)). Thus, ^{13}C CP-MAS NMR spectra highlight both disappearance of the alkyne, ν(C≡C), resonance at 80 ppm, indicative of completion of the [2+2] cycloaddition reaction, and appearance of resonances at 29 and 44 ppm from the integrated TCNQ moieties. Fitting the N_2 adsorption isotherm to the Brunauer-Emmett-Teller (BET) equation resulted in a surface area of 812 m^2/g for TCNQ[**1≡(50%)**] (Figure 1.21). The cyclic voltammogram is shown in Figure 1.1. Conductivity studies were performed and shown in Figure 1.4. The FTIR and diffuse reflectance spectra, gas sorption analysis plot, emission spectra, and PXRD pattern are shown in Figures 1.1, 1.4, 1.21, 1.32, and 1.33. To further study the reaction between TCNQ derivative and the COF, we employed diffuse reflectance (DR), steady-state and time-resolved photoluminescence, and X-ray photoelectron spectroscopies, as well as conductivity measurements. Integration of acceptor units inside the COF resulted in a significant color change from yellow to red. A DR spectroscopic analysis revealed that integration of TCNQ-based electron acceptors resulted in appearance of an additional absorption band (Figure 1.4), which can be attributed to charge transfer between the COF and TCNQ. The analysis of time-resolved PL decay curves revealed an amplitude-averaged lifetime of 103 ps for TCNQ[**1≡(50%)**] in comparison with 496 ps for the COF itself (Figure 1.4). In addition, the presence of an electron acceptor, such as TCNQ derivatives in the COF structure, resulted in complete PL quenching (Figure 1.31).

For additional evidence of complete integration of acceptor-containing materials in the COF (i.e., all –C≡C are occupied with acceptor molecules), we devised a strategy to target any remaining alkyne sites within the COF using a fluorescent tag. In the case of remaining unreacted alkyne sites, the fluorescent tag will bind to the COF, which can be easily detected through the appearance of emission. In contrast, if all reactive sites are occupied, then no changes in emission/absorption profile would be detected. Experimental details are described below.

Development of Synthetic Conditions for Sonogashira Coupling Reactions.

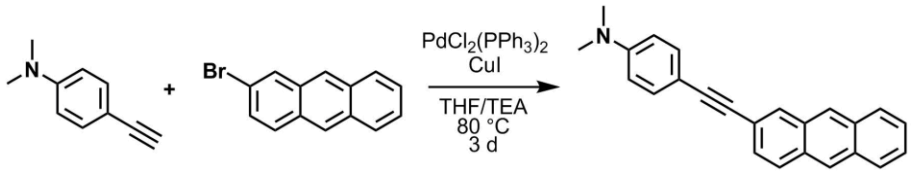

For investigation of reaction conditions necessary to perform a Sonogashira coupling using 2-bromoanthracene with **1≡(50%)**, the conditions were first studied with molecular species. In a 50-mL Schlenk flask, 2-bromoanthracene (50 mg, 0.19 mmol), 4-ethynyl-*N*,*N*-dimethylaniline (42 mg, 0.29 mmol), $PdCl_2(PPh_3)_2$ (14 mg, 0.019 mmol), and CuI (4 mg, 0.019 mmol) were added. Degassed triethylamine (10 mL) and THF (10 mL) were added to the flask, and the mixture was stirred at 80 °C for 3 d. Upon cooling to room temperature, the solvent was evaporated, and the sample was subjected to purification using preparative thin layer chromatography (SiO_2, hexane:DCM (1:1)). A yield of 62% was obtained. ^{1}H NMR ($CDCl_3$, 300 MHz): δ = 8.38 (2H, s), 8.18 (1H, s), 7.99-7.94 (3H, m), 7.55-7.46 (5H, m), 6.71 (2H, d, J = 8.94), and 3.03 (6H, s) ppm (Figure 1.18). ^{13}C NMR ($CDCl_3$, 101 MHz): δ = 150.19, 132.84, 132.07, 131.95, 131.32, 130.88, 130.53, 128.23, 128.20, 128.09, 127.92, 126.15, 126.02, 125.62, 125.58, 120.93,

111.88, 110.03, 91.75, 88.18, and 40.24 ppm (Figure 1.18). HRMS (ESI, m/z) calculated for $C_{24}H_{19}N$ $[M+H]^+$ 322.1587, found 322.1590.

Development of the Synthetic Conditions for Fluorescent Labeling of Unreacted Active Sites.

Initially, we tested the concept on **1≡(50%)** using two fluorophores, 6-bromo-3-cyano-4-methylcoumarin and 2-bromoanthracene, and then re-applied this concept for the compound of interest, TCNQ[**1≡(50%)**]. Thus, we coupled **1≡(50%)** with fluorophores using a modified literature procedure, [51] and determined reaction progress by FTIR spectroscopy in order to establish a baseline for fluorescent response (control experiments). The experimental details for the control experiments and reactions with TCNQ[**1≡(50%)**] for the two fluorophores are given below.

*Synthesis of anthracene**[1≡(50%)]**.*

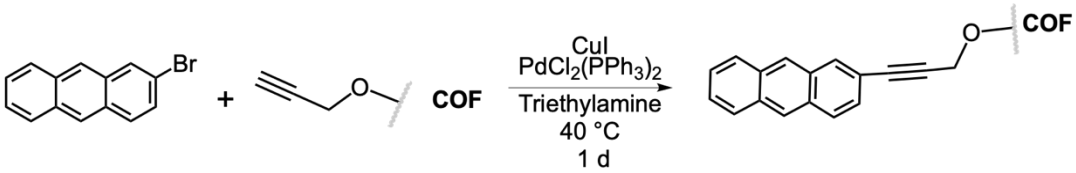

In a 25-mL three-neck round bottom flask, **1≡(50%)** (32 mg), 2-bromoanthracene (2.0 mg, 0.078 mmol), bistriphenylphosphinepalladium(II) dichloride (5.0 mg, 0.0071 mmol), and CuI (2.0 mg, 0.011 mmol) were added. Degassed triethylamine (10 mL, 0.072 mmol) was added to the flask and the mixture was stirred at 40 °C for 1 d. Upon cooling to room temperature, the precipitate was collected, washed with THF/ACN/DCM, and dried under vacuum overnight to afford an orange solid in a quantitative yield. FTIR (neat, cm^{-1}): 2962, 2149, 1613, 1591, 1505, 1488, 1465, 1443, 1409, 1374, 1289, 1209, 1180, 1147, 1039, 1013, 974, 879, 828, 733, and 693 (Figure 1.34). The FTIR data shown in Figure 1.34 highlight the preservation of the ν(C≡C) band

and disappearance of the ν(H–C≡C) band-, indicating transformation of all terminal alkynes to internal alkynes. The PXRD pattern is shown in Figure 1.33. Coupling of the fluorophore with the COF resulted in a significant color change of the material from yellow to orange. Emission and DR spectra are shown in Figures 1.27 and 1.29. Non-integrated 2-bromoanthracene is almost non-emissive in the solid state, which is in line with literature reports.[52-53] More importantly, integration of anthracene derivative inside the COF matrix resulted in appearance of a strong emission with λ_{max} = 658 nm (λ_{ex} = 365 nm).

*Synthesis of 4-methyl-2-oxo-2H-chromene-3-carbonitrile **[1≡(50%)]**.*

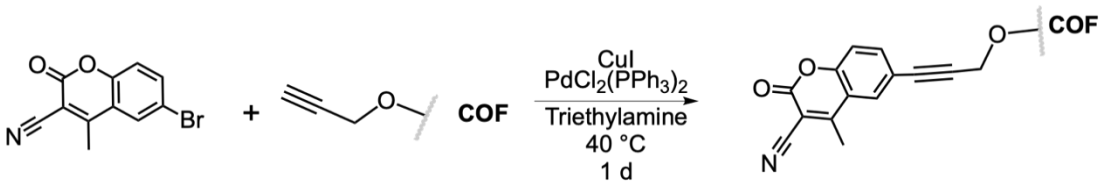

In a 25-mL three-neck round bottom flask, **1≡(50%)** (32 mg), 6-bromo-3-cyano-4-methylcoumarin (22 mg, 0.083 mmol), bistriphenylphosphinepalladium(II) dichloride (5.0 mg, 0.0071 mmol), and CuI (0.0020 g, 0.011 mmol) were added. Degassed triethylamine (10 mL, 0.072 mmol) was added to the flask and the mixture was stirred at 40 °C for 1 d. Upon cooling to room temperature, the precipitate was collected, washed with THF/ACN/DCM, and dried under vacuum overnight to give an orange solid in a quantitative yield. FTIR (neat, cm^{-1}): 2960, 2160, 1734, 1591, 1505, 1486, 1465, 1408, 1289, 1208, 1181, 1144, 1080, 1030, 875, 825, and 693 (Figure 1.35). The FTIR data in Figure 1.35 highlight the preservation of the ν(C≡C) band and disappearance of the ν(H–C≡C) band, indicating transformation of all terminal alkynes to internal alkynes. We also observed appearance of the carbonyl band, ν(-C=O), as an additional indication that

coumarin was coupled to the framework (Figure 1.35). The PXRD pattern is shown in Figure 1.33. Coupling of the fluorophore with the COF resulted in a significant color change of the material from yellow to brown. The coumarin-integrated scaffold also exhibited an increase in emission. Emission and DR spectra are shown in Figures 1.28 and 1.30. Non-integrated 6-bromo-3-cyano-4-methylcoumarin is non-emissive in the solid state which is in line with literature reports.[54-55] Integration of coumarin derivative inside the COF matrix resulted in appearance of a strong emission with λ_{max} = 652 nm (λ_{ex} = 365 nm).

*Synthesis of 2-bromoanthracene@TCNQ**[1≡(50%)]**.*

In a 25-mL three-neck round bottom flask, TCNQ[**1≡(50%)**] (32 mg), 2-bromoanthracene (2.0 mg, 0.078 mmol), bistriphenylphosphinepalladium(II) dichloride (5.0 mg, 0.0071 mmol), and CuI (2.0 mg, 0.011 mmol) were added. Degassed triethylamine (10 mL, 0.072 mmol) was added to the flask and the mixture was stirred at 40 °C for 1 d. Upon cooling to room temperature, the precipitate was collected, washed with THF/ACN/DCM, and dried under vacuum overnight to give a brown solid in a quantitative yield. FTIR (neat, cm^{-1}): 2938, 2834, 2180, 2136, 1590, 1505, 1488, 1465, 1444, 1409, 1375, 1290, 1247, 1209, 1175, 1144, 1040, 1012, 976, 925, 876, 827, 732, and 694 (Figure 1.35). The FTIR spectra shown in Figure 1.36 highlight the preservation of nitrile band, ν(C≡N), indicating that TCNQ moities remained covalently bound to the framework. As expected, there was no appearance of any additional resonances. In addition, no color change (previously observed for anthracene[**1≡(50%)**]) was detected in this case. Moreover, absence of coupling of the fluorophore with TCNQ[**1≡(50%)**] was confirmed by lack of changes in the emission and absorption profiles (Figure 1.29). The

PXRD pattern is shown in Figure 1.33. In contrast to moderate crystallinity loss observed in the case of anthracene[**1≡(50%)**], the PXRD pattern of TCNQ[**1≡(50%)**] after "treatment" with 2-bromoanthracene still indicates high sample crystallinity (similar to as-synthesized TCNQ[**1≡(50%)**]) which can be used as an additional evidence of absence of reactive alkyne species (Figure 1.33).

Combination of the results observed in the case of fluorophore tag treatment with solid-state NMR and FTIR spectroscopic data indicate that all accessible alkyne sites are occupied by TCNQ-based moieties in the COFs (Figures 1.4 and 1.36).

*Synthesis of 6-bromo-3-cyano-4-methylcoumarin@TCNQ**[1≡(50%)]**.*

In a 25-mL three-neck round bottom flask, TCNQ[**1≡(50%)**] (32 mg), 6-bromo-3-cyano-4-methylcoumarin (0.022 g, 0.083 mmol), bistriphenylphosphinepalladium(II) dichloride (0.0050 g, 0.0071 mmol), and CuI (0.0020 g, 0.011 mmol) were added. Degassed triethylamine (10 mL, 0.072 mmol) was added to the flask and the mixture was stirred at 40 °C for 1 d. Upon cooling to room temperature, the precipitate was collected, washed with THF/ACN/DCM, and dried under vacuum overnight to give a brown solid in a quantitative yield. FTIR (neat, cm^{-1}): 2941, 2163, 2136, 1590, 1506, 1490, 1467, 1444, 1375, 1292, 1211, 1180, 1144, 1041, 1013, 977, 926, 877, 828, 732, and 695. The FTIR data are shown in Figure 1.36, which highlights the preservation of ν(C≡N)band, indicating that TCNQ moieties remained covalently bound to the framework. As expected, there was no appearance of any additional resonances. In addition, no color change (previously observed for 4-methyl-2-oxo-2*H*-chromene-3-carbonitrile[**1≡(50%)**]) was detected in this case. Moreover, absence of coupling of the fluorophore with TCNQ[**1≡(50%)**] was confirmed by lack of changes in the emission and absorption

profiles (Figure 1.29). The PXRD pattern is shown in Figure 1.33. In contrast to moderate crystallinity loss observed in the case of 4-methyl-2-oxo-2*H*-chromene-3-carbonitrile[**1≡(50%)**], the PXRD pattern of TCNQ[**1≡(50%)**] after "treatment" with 6-bromo-3-cyano-4-methylcoumarin still indicates high sample crystallinity (similar to as-synthesized TCNQ[**1≡(50%)**]), which can be used as additional support for the absence of reactive alkyne species (Figure 1.33).

Combination of the results observed in the case of fluorophore tag treatment with solid-state NMR and FTIR spectroscopic data indicate that all accessible alkyne sites are occupied by TCNQ-based moieties in the prepared COFs (Figures 1.4 and 1.36).

*Preparation of I_2@**[1≡(50%)]**, I_2@NEM-C_{60}**[1≡(34%)]**, I_2@TCNQ**[1≡(50%)]**, and I_2@TCNQ**[1≡(100%)]**.*

Preparation of iodine doped frameworks, I_2@[**1≡(50%)**], I_2@NEM-C_{60}[**1≡(34%)**], I_2@TCNQ[**1≡(50%)**], and I_2@TCNQ[**1≡(100%)**], was performed based on a modified literature procedure.[56] An uncapped 0.5 dram vial containing the COF (15 mg) was placed inside a 20 mL vial charged with iodine (100 mg, 0.39 mmol) and subsequently sealed for three days. The iodine-doped materials were then subjected to pressed-pellet conductivity measurements (see the section *Physical Measurements*).

X-Ray Structure Determination, $C_{22}H_{15}N_5$.

X-ray intensity data from a black plate were collected at 100(2) K using a Bruker D8 QUEST diffractometer equipped with a PHOTON-100 CMOS area detector and an Incoatec microfocus source (Mo Kα radiation, λ = 0.71073 Å). The raw area detector data frames were reduced and corrected for absorption effects using the Bruker APEX3, SAINT+ and SADABS programs.[57-58] The structure was solved with SHELXT.[59-60]

Subsequent difference Fourier calculations and full-matrix least-squares refinement against F^2 were performed with SHELXL-2018[59-60] using OLEX2.[61]

The compound crystallizes in the space group *P*-1 (No. 2) of the triclinic system. The asymmetric unit consists of one $C_{22}H_{15}N_5$ molecule and half of one benzene molecule. The benzene is located on a crystallographic inversion center. All non-hydrogen atoms were refined with anisotropic displacement parameters. Hydrogen atoms bonded to carbon were located in difference Fourier maps before being placed in geometrically idealized positions and included as isotropically refined riding atoms with d(C–H) = 0.95 Å for aromatic hydrogen atoms and d(C–H) = 0.98 Å for methyl hydrogens. The methyl hydrogens were allowed to rotate as a rigid group to the orientation of maximum observed electron density. The largest residual electron density peak in the final difference map is 0.46 e/Å^3, located 1.00 Å from C25.

Table 1.1. X-ray structure refinement data for $C_{22}H_{15}N_5 \cdot (C_6H_6)_{0.5}$.[a]

formula	$C_{25}H_{18}N_5$
FW	388.44
T, K	100(2)
crystal system	triclinic
space group	P-1
Z	2
a, Å	7.8843(3)
b, Å	9.0131(3)
c, Å	15.2276(5)
α, °	72.9600(10)
β, °	76.2080(10)
γ, °	81.434(2)
V, Å^3	1001.12(6)
d_{calc}, g/cm^3	1.289
μ, mm^{-1}	0.079
F(000)	406.0
crystal size, mm^3	0.4 × 0.26 × 0.18
theta range	4.744 to 60.27
index ranges	–11 ⩽ h ⩽ 11

	$-12 \leqslant k \leqslant 12$ $-21 \leqslant l \leqslant 21$
refl. collected	74218
data/restraints/ parameters	5887/0/292
GOF on F^2	1.027
R_1/wR_2, $[I>=2\sigma(I)]^b$	0.0416/0.1113

[a] Mo-K_α (λ = 0.71073Å) radiation
[b] $R_1 = \Sigma||F_o| - |F_c||/ \Sigma |F_o|$, $wR_2 = \{\Sigma [w(F_o^2 - F_c^2)^2]/ \Sigma [w(F_o^2)^2]\}^{1/2}$

Fluorescence spectroscopy.

An Edinburgh FS5 fluorescence spectrometer equipped with a 150 W Continuous Wave Xenon Lamp source for excitation was used to acquire steady-state emission spectra. Emission measurements on solid samples were collected on powders of the desired materials placed inside a 0.5 mm quartz sample holder using the front-facing module. Fluorescence lifetimes were measured using a Mini-τ lifetime spectrometer from Edinburgh Instruments equipped with a 365-nm picosecond-pulsed-light-emitting diode (EPLED 365).

Fitting of fluorescence decays.

The fluorescence decays for **1≡(34%)**, NEM-C_{60}[**1≡(34%)**], and TCNQ[**1≡(50%)**] were fit with the triexponential function:

$$I(t) = \int_{-\infty}^{t} IRF(t') \sum_{i=1}^{n} B_i e^{\left[-\frac{t-t'}{\tau_i}\right]} dt'$$

where τ and B are lifetime and amplitude, respectively.

The amplitude-weighted average fluorescence lifetimes were calculated based on the following equation:

$$\langle \tau_{av} \rangle = \frac{B_1\tau_1 + B_2\tau_2 + B_3\tau_3}{B_1 + B_2 + B_3}$$

	B_1	τ_1, ns	B_2	τ_2, ns	B_3	τ_3, ns	$\langle\tau_{av}\rangle$, ns
1≡(34%)	0.0424	0.291	0.0831	0.568	0.0152	0.681	0.496
NEM-C_{60}[**1≡(34%)**]	1.77	0.0120	0.135	0.0751	0.0005	59.4	0.032
TCNQ[**1≡(50%)**]	0.466	0.057	0.116	0.186	0.0159	0.869	0.103

Physical Measurements.

NMR spectra were obtained on Bruker Avance III-HD 300 and Bruker Avance III 400 MHz NMR spectrometers. ^{13}C and ^{1}H NMR spectra were referenced to natural abundance ^{13}C peaks and residual ^{1}H peaks of deuterated solvents, respectively. FTIR spectra were collected on a Perkin-Elmer Spectrum 100. Powder X-ray diffraction patterns were recorded from a Rigaku Miniflex II diffractometer with an accelerating voltage and current of 30 kV and 15 mA, respectively. Thermogravimetric analysis was performed on an SDT Q600 Thermogravimetric Analyzer using an alumina boat as the sample holder. Diffuse reflectance spectra were collected on a PerkinElmer Lambda 45 UV-vis spectrometer referenced to Spectralon®. The BET specific surface area was determined by measuring N_2 adsorption at 75.6 K using a Micromeritics ASAP 2020. Prior to gas sorption measurement, the NEM-C_{60}[**1≡(34%)**] sample was solvent exchanged with benzene for three days, tetrahydrofuran for one day, then heated in vacuum (1.0×10^{-7} Torr) with a heating rate of 1 °C/min up to 65 °C, held for twelve hours, subsequently heated at 75 °C at 10 °C/min, and held at this temperature for twelve hours. Prior to gas sorption measurement of **1≡(34%)** and TCNQ[**1≡(50%)**], the samples were heated in vacuum (1.0×10^{-7} Torr) with a heating rate of 1 °C/min up to 60 °C, held

for three hours, and subsequently heated at 80 °C at 10 °C/min, then held at this temperature for nine hours. Wide-Angle X-ray Scattering (WAXS) experiments were conducted using a SAXSLab Ganesha at the South Carolina SAXS collaborative (SCSC). A Xenocs GeniX 3D microfocus source was used with a copper target to produce a monochromatic beam with a 0.154 nm wavelength. The instrument was calibrated just before measurement, using the National Institute of Standards and Technology reference material, 640c silicon powder with the peak position at $2\theta = 28.44°$, where 2θ is the total scattering angle. A Pilatus 300k detector (Dectris) was used to collect the two-dimensional (2D) scattering pattern with nominal pixel dimensions of $172 \times 172\ \mu m^2$. The SAXS data were acquired with an X-ray flux of ~4.1 M photon per s incident upon the sample and a detector-to-sample distance of 1040 mm. The transmission SAXS data were measured to observe the purely in-plane morphology. The 2D images were azimuthally integrated to yield the scattering vector and intensity. Peak positions were fitted using custom MATLAB software.[62]

Cyclic voltammetry (CV) measurements were carried out in anhydrous *N*,*N*-dimethylformamide (DMF) or anhydrous acetonitrile (ACN) solution using a WaveDriver 20 Bipotentiostat combined with the Aftermath software. For measurements of TCNQ, C_{60}, and NEM-C_{60}, all solutions contained 0.1 M tetrabutylammonium hexafluorophosphate and 0.5 mM analyte, and measurements were performed in a glass solution reservoir equipped with saturated calomel reference, platinum wire counter, and glassy carbon or gold working electrodes. In order to perform CV measurements on TCNQ[**1≡(50%)**] and NEM-C_{60}[**1≡(34%)**], modification of the electrochemical setup was necessary. The working electrode was modified with a COF slurry prepared by

grinding TCNQ[**1≡(50%)**] or NEM-C_{60}[**1≡(34%)**] (40 wt.%) and carbon black (60 wt.%) with 0.1 mL of Nafion. The slurry was then pipetted onto the tip of the electrode and dried overnight under high vacuum before use.

Cyclic voltammetry of TCNQ itself (1.0×10^{-4} M) in a 0.1 M solution of tetrabutylammonium hexafluorophosphate in acetonitrile afforded one reversible reduction at E_p = –0.5 V and one reversible oxidation at 0.1 V (Figure 1.23). Comparison of the acquired CV data for TCNQ[**1≡(34%)**] to TCNQ itself, shows that potentials of TCNQ[**1≡(34%)**] are less negative at E_p = –0.3 V and 0.2 V vs. SCE (Figure 1.4). In DMF, C_{60} exhibits four reversible reduction waves at E_p = –0.3 V, –0.7 V, –1.4 V, and –1.9 V vs. SCE (Figure 1.22). In comparison with parent C_{60}, NEM-C_{60} exhibits two quasi-reversible reductions in DMF at E_p = –0.9 V and –1.8 V vs. SCE (Figure 1.24). The redox potentials of NEM-C_{60} and NEM-C_{60}[**1≡(34%)**] (–1.2 V and –2.1 V vs. SCE) are also similar (Figure 1.25), with a slight shift in potential, highlighting the inclusion of NEM-C_{60} and reinforcement of the redox active nature within the COF. As a control experiment, CVs of the COF itself and carbon black were measured in which no redox activity was found (Figure 1.26).

A two-point method was employed to measure conductance σ (S/cm) of pressed pellets according to following equation:

$$\sigma = Il/VA,$$

where I - current, l - thickness of the pellets, V - voltage, A - surface area of the prepared pellets.

The electrical conductance in the prepared materials follows Ohm's law and was measured by fitting a linear current (I)-voltage (V) curve obtained by using a source

meter (Keithley Instruments GmbH, Germering, Germany, model 263) and an electrometer (Keithley Instruments GmbH, Germering, Germany, model 617).[63-64] All samples were prepared consistently by using the same amount of materials (30 mg of material, dried overnight on the vacuum) and the same pressing technique (material was pressed under 4000 psi at room temperature for five minutes with an International Crystal Laboratory 20 Ton E-Z Hydraulic Laboratory PressTM), which relieves the issue of deviations from the ideal configuration. A home-built setup was used to perform two-contact probe conductivity measurements on the pressed pellets: the pellet was placed between two brass plates with attached contacts. A layer of double-sided carbon tape (Electron Microscopy Sciences) was added between a pellet and plates to improve contact.

Solid-state NMR spectra (^{13}C CP-MAS) were collected on a Bruker Avance III-HD 500 MHz spectrometer fitted with a 1.9 mm MAS probe. $^{13}C\{^{1}H\}$ CP-MAS NMR spectra (125.79 MHz) were collected at ambient temperature with a sample rotation rate of 20 kHz. For cross polarization, 2.0 ms contact time with linear ramping on the ^{1}H channel and 62.5 kHz field on the ^{13}C channel were used. ^{1}H dipolar decoupling was performed with SPINAL64 modulation and 147 kHz field strength. Free induction decays (2048-5000 transients) were collected with a 27 ms acquisition time over a 400 ppm spectra width with a relaxation delay of 2.0 s. All XPS experiments were carried out with a Kratos AXIS Ultra DLD system, which was equipped with a monochromatic AlK_{α} source, a hemispherical analyzer, a charge neutralizer for studying insulating samples, and a load lock chamber for rapid introduction of samples into the vacuum chamber. This system has been described in more detail elsewhere.[63-64] Dwell times were 1000 ms and

600 ms for the valence band and C(1s) regions, respectively, and the step size for both regions was 0.06 eV.

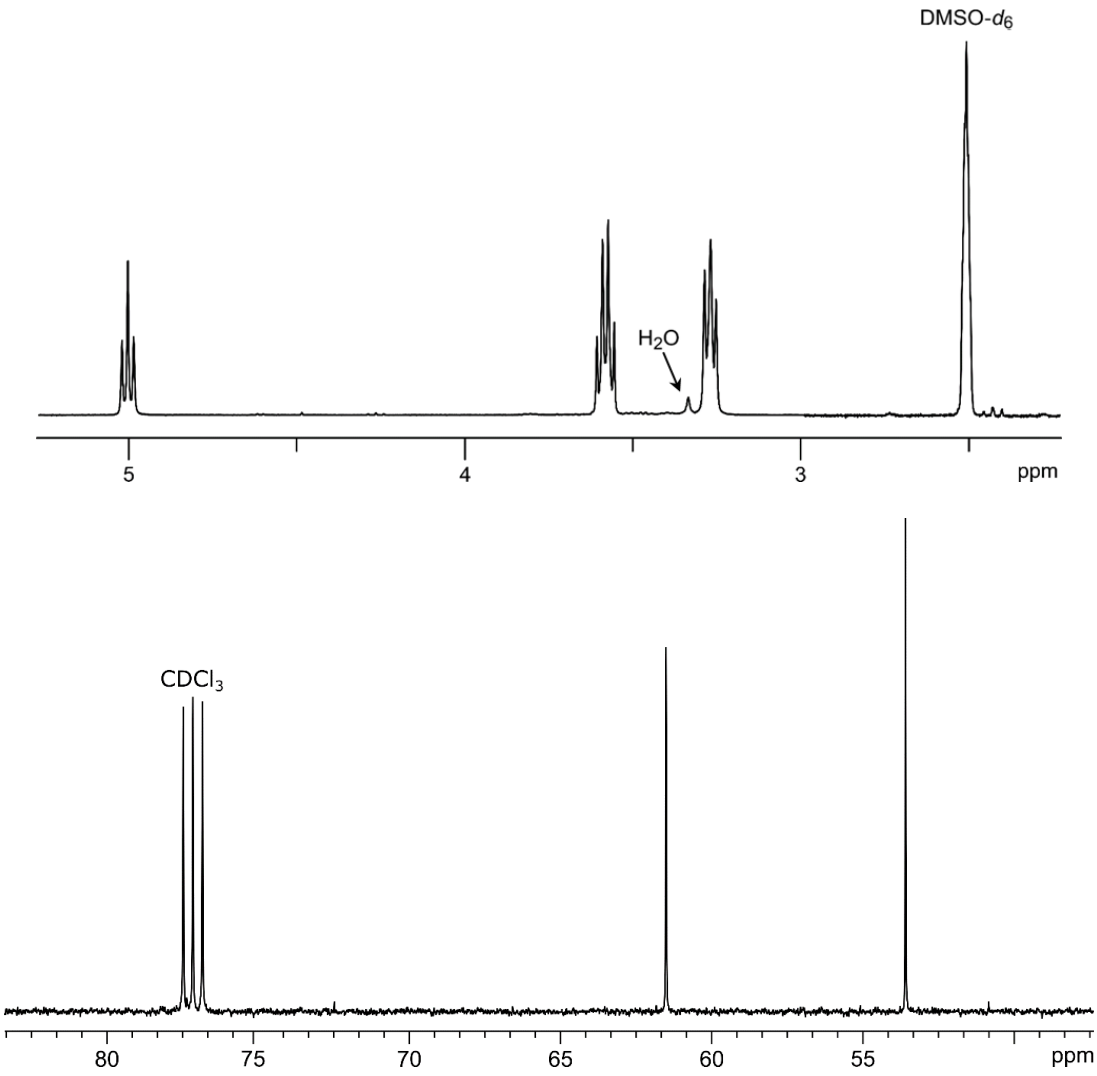

Figure 1.5. ^{1}H NMR (*top*) spectrum of 2-azidoethanol in DMSO-d_6 and ^{13}C NMR (*bottom*) spectrum of 2-azidoethanol in $CDCl_3$.

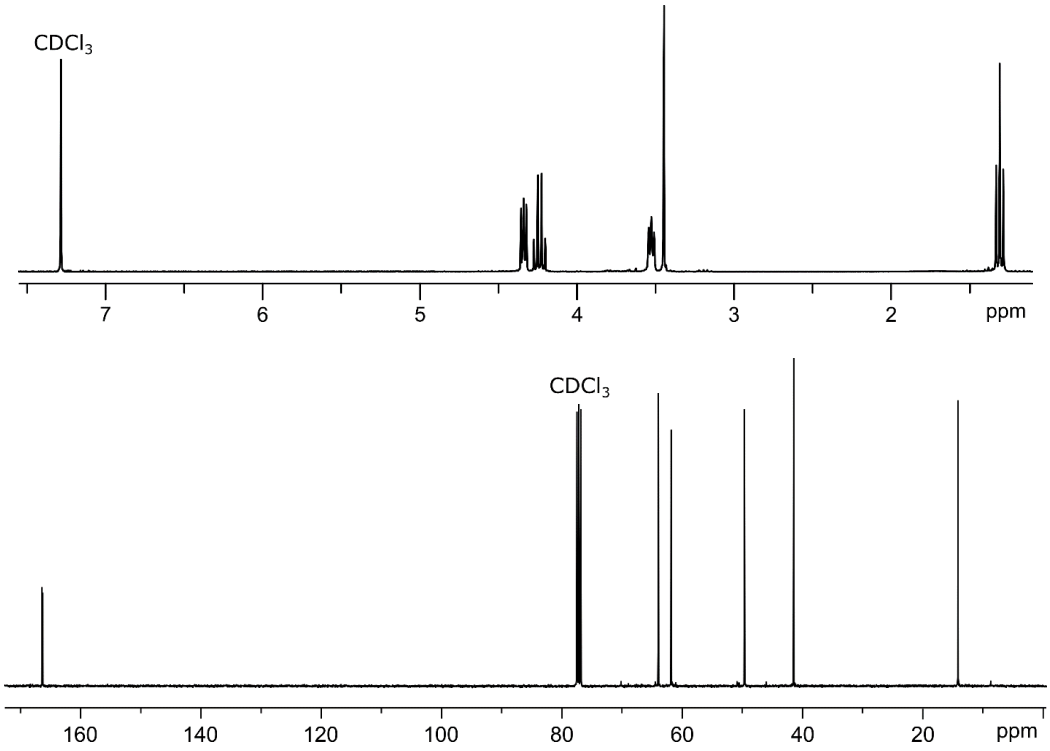

Figure 1.6. ^{1}H NMR (*top*) and ^{13}C NMR (*bottom*) spectra of NEM in $CDCl_3$.

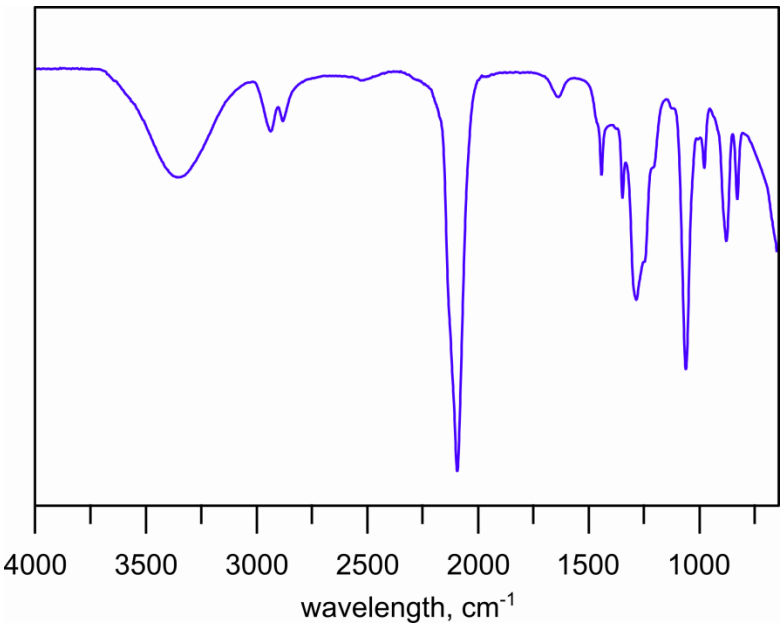

Figure 1.7. FTIR spectrum of 2-azidoethanol.

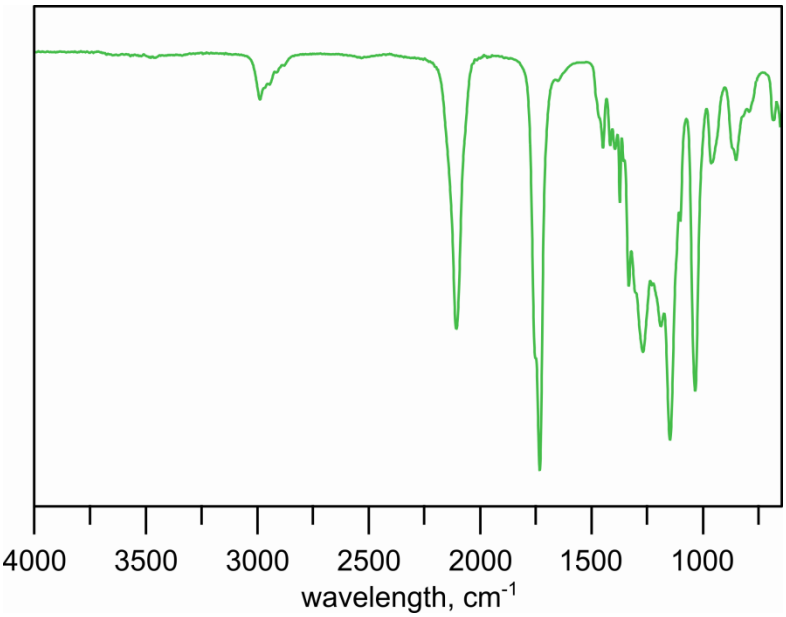

Figure 1.8. FTIR spectrum of NEM.

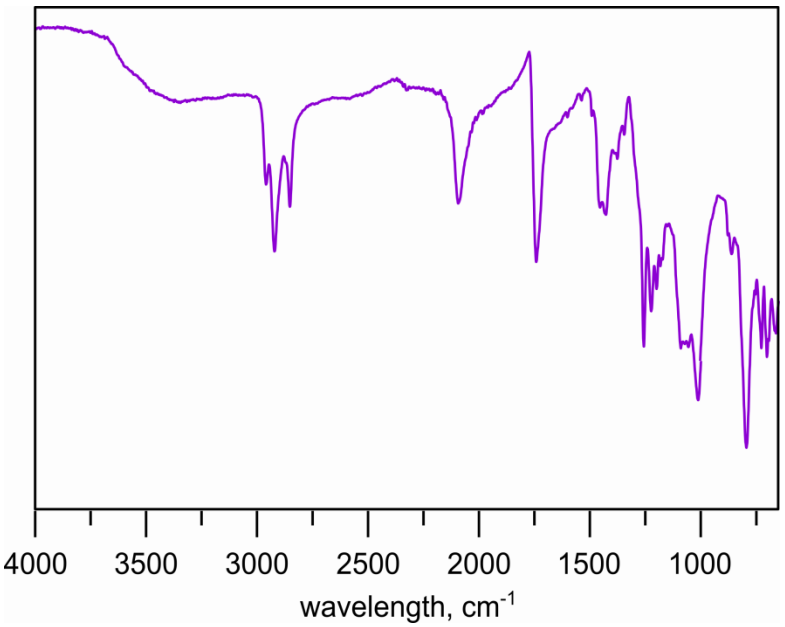

Figure 1.9. FTIR spectrum of NEM-C_{60}.

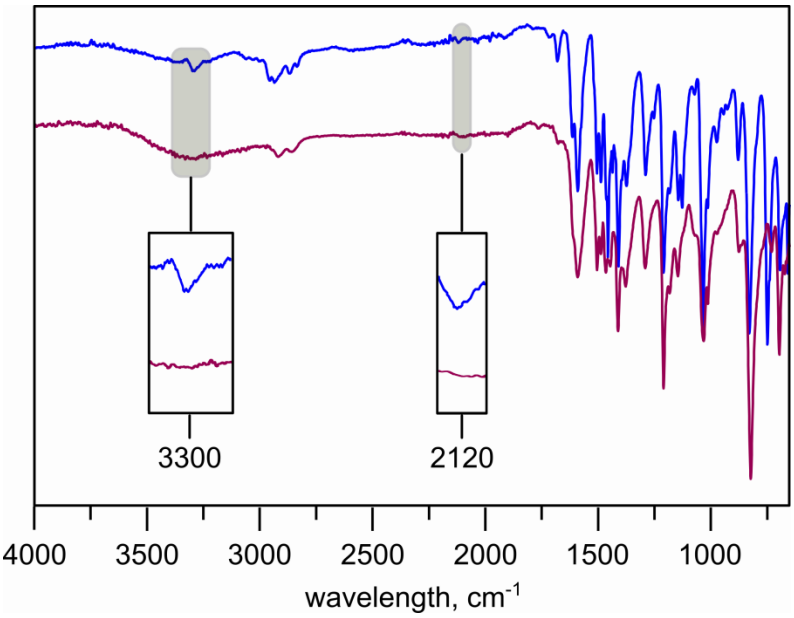

Figure 1.10. FTIR spectra of **1≡(34%)** (blue) and 2-azidoethanol[**1≡(34%)**] (red). The grey areas highlight the disappearance of both the H–C≡C (3300 cm^{-1}) and the C≡C (2120 cm^{-1}) stretches in 2-azidoethanol[**1≡(34%)**].

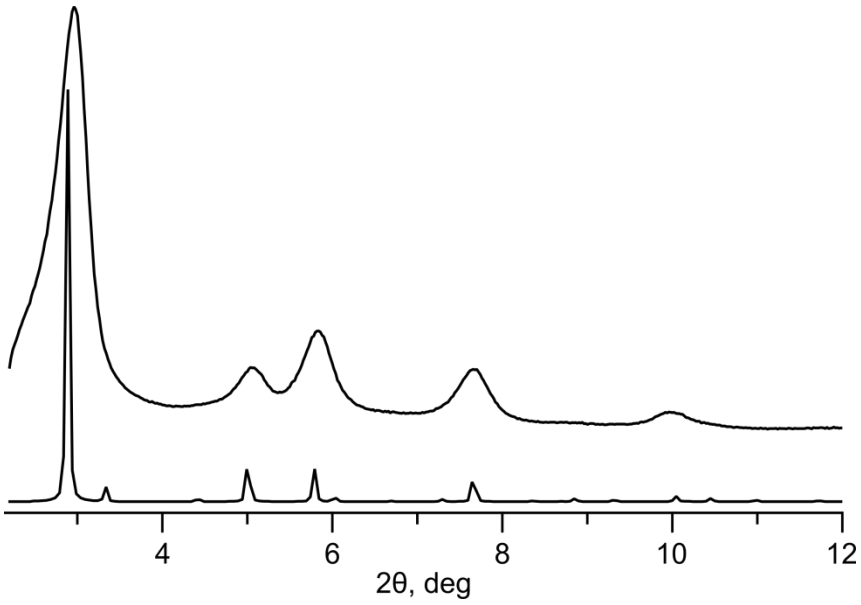

Figure 1.11. PXRD pattern of **1≡(34%)** (top) and simulated pattern (bottom).

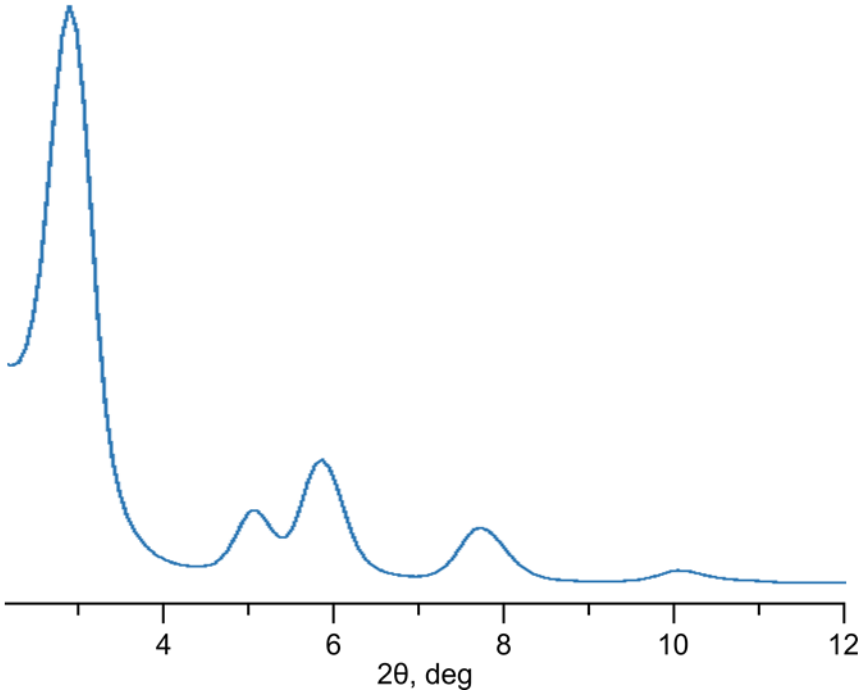

Figure 1.12. WAXS pattern of **1≡(34%)**.

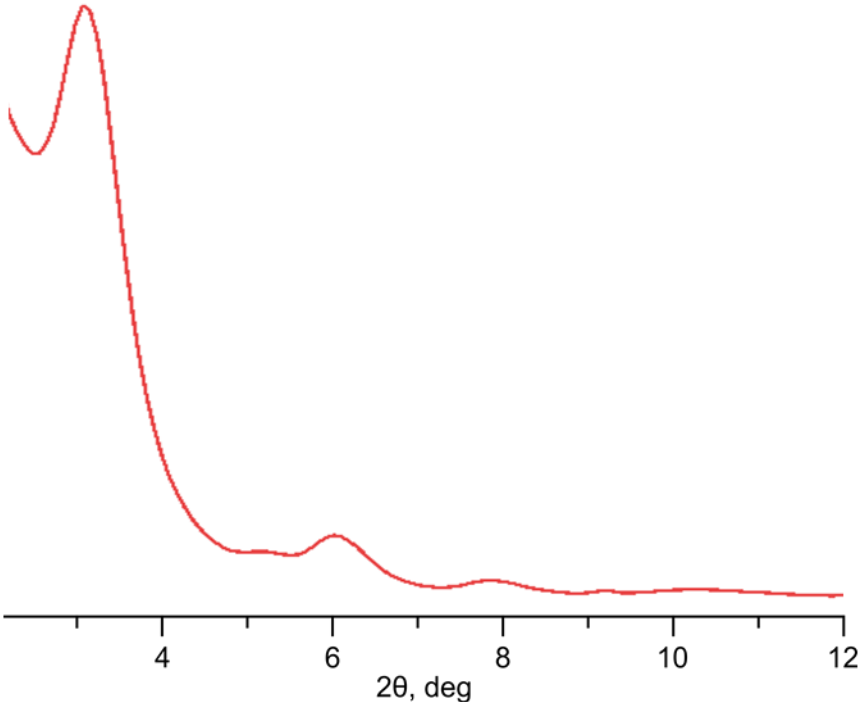

Figure 1.13. WAXS pattern of NEM**[1≡(34%)]**.

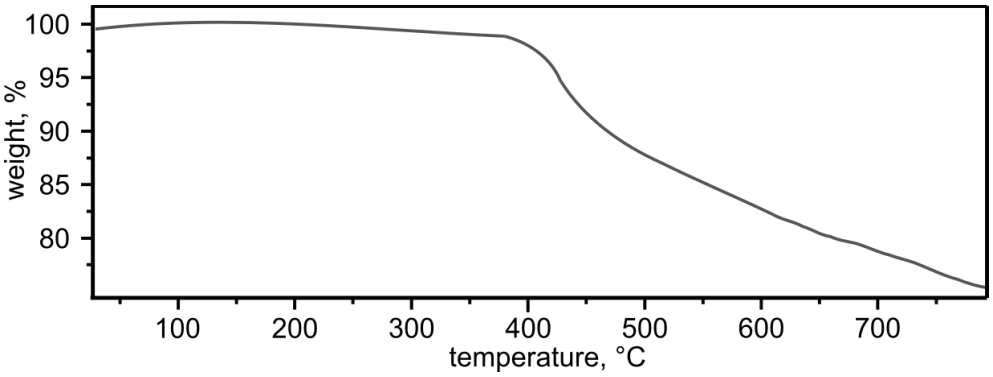

Figure 1.14. Thermogravimetric analysis plot of **1≡(34%)**.

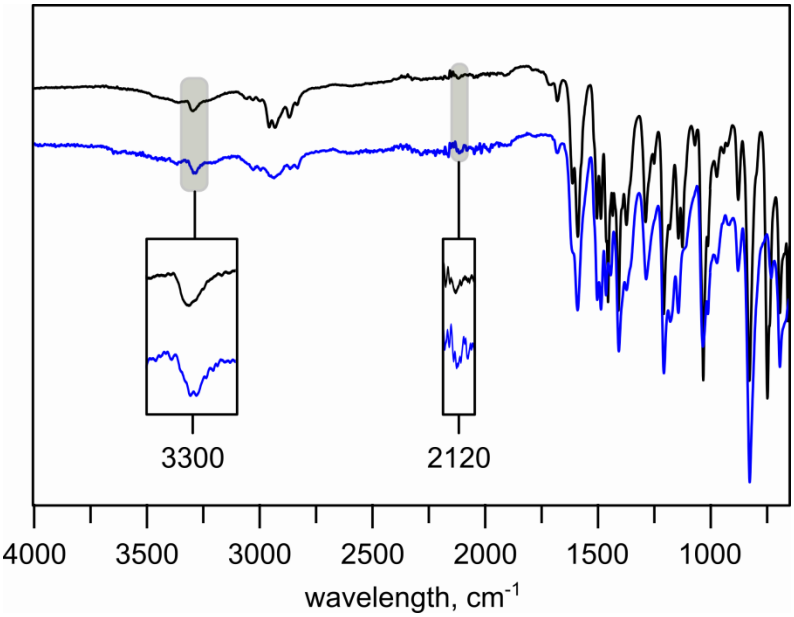

Figure 1.15. FTIR spectrum of **1≡(34%)** (black) and a control experiment involving **1≡(34%)** (blue). The grey areas highlight the conservation of the H–C≡C (3300 cm^{-1}) and the C≡C (2120 cm^{-1}) stretches in the control experiment performed with **1≡(34%)**, showing that the alkynes within the structure were not affected.

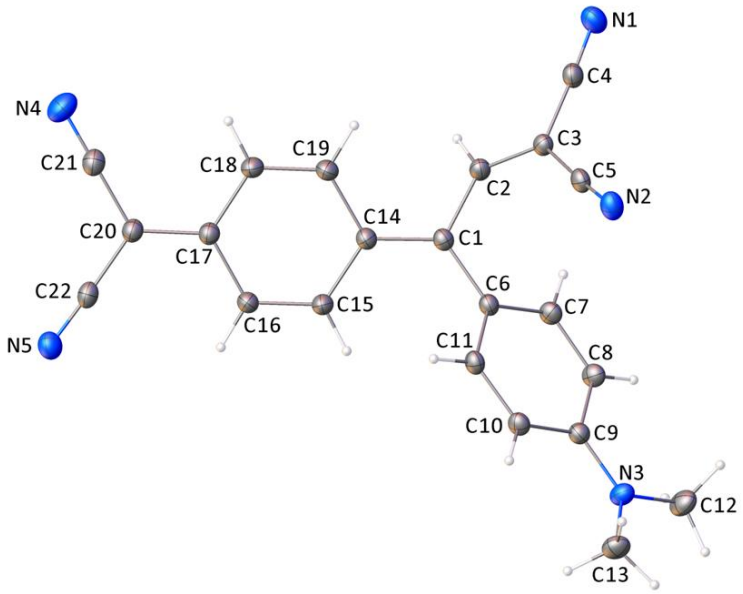

Figure 1.16. Crystal structure of $C_{22}H_{15}N_5$. Displacement ellipsoids are drawn at the 50% probability level. Blue, grey, and white spheres correspond to nitrogen, carbon, and hydrogen, respectively.

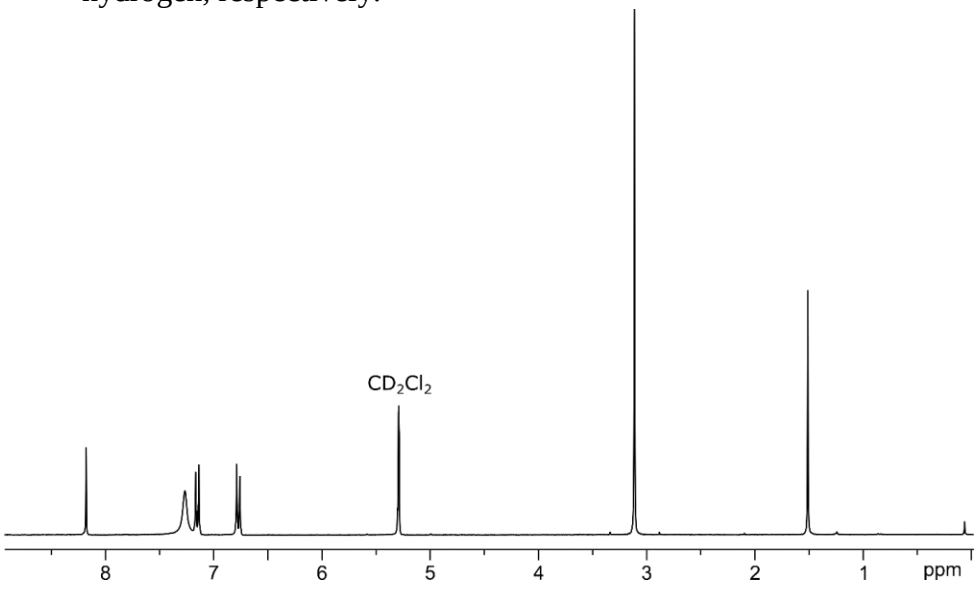

Figure 1.17. ^{1}H NMR spectrum of TCNQ-based molecular click in CD_2Cl_2.

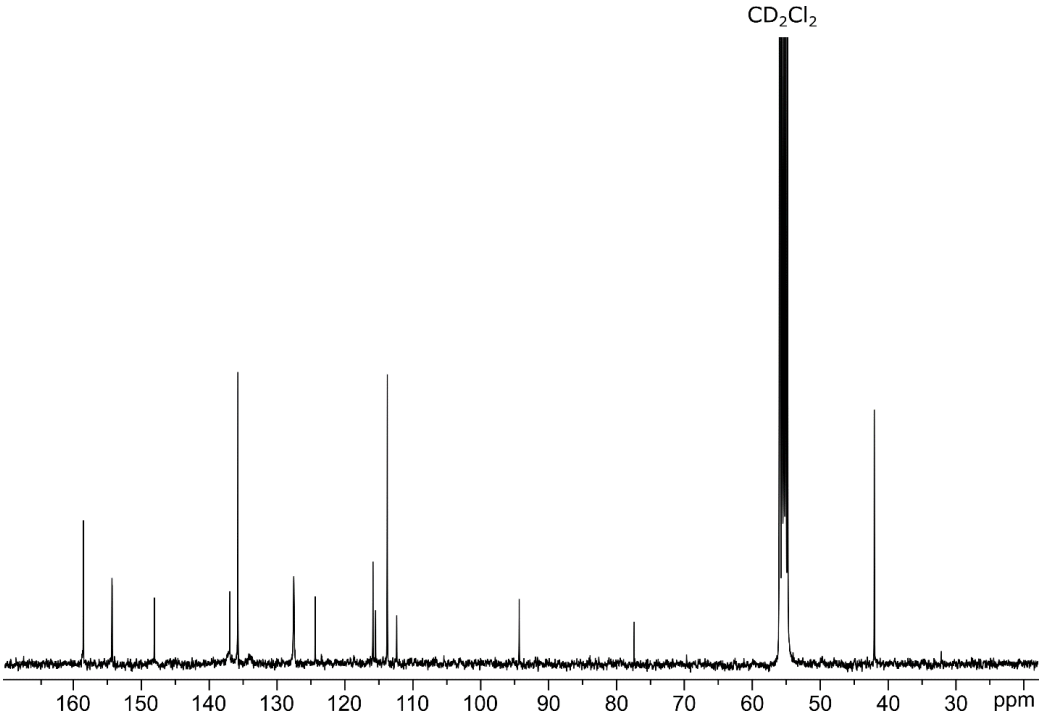

Figure 1.18. ^{13}C NMR spectrum of TCNQ-based molecular click in CD_2Cl_2.

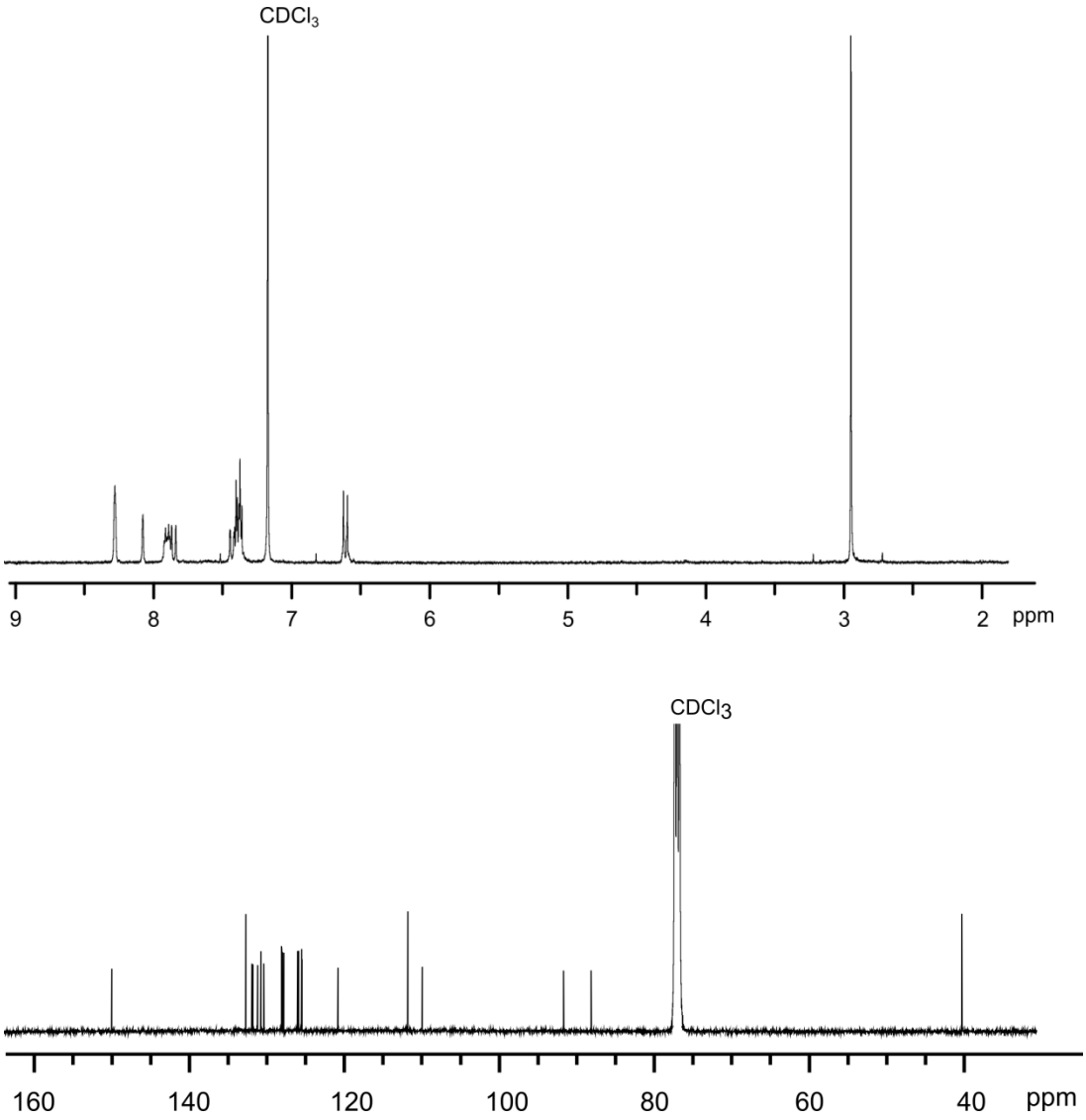

Figure 1.19. ^{1}H NMR (*top*) and ^{13}C NMR (*bottom*) spectra of 4-(anthracen-2-ylethynyl)-*N*,*N*-dimethylaniline in $CDCl_3$.

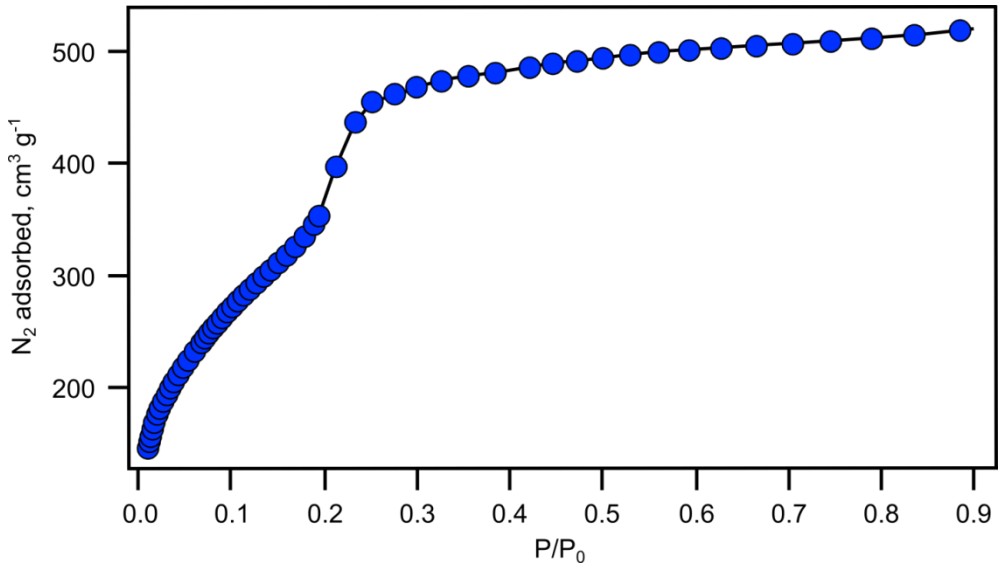

Figure 1.20. N_2 adsorption isotherm of **1≡(34%)**.

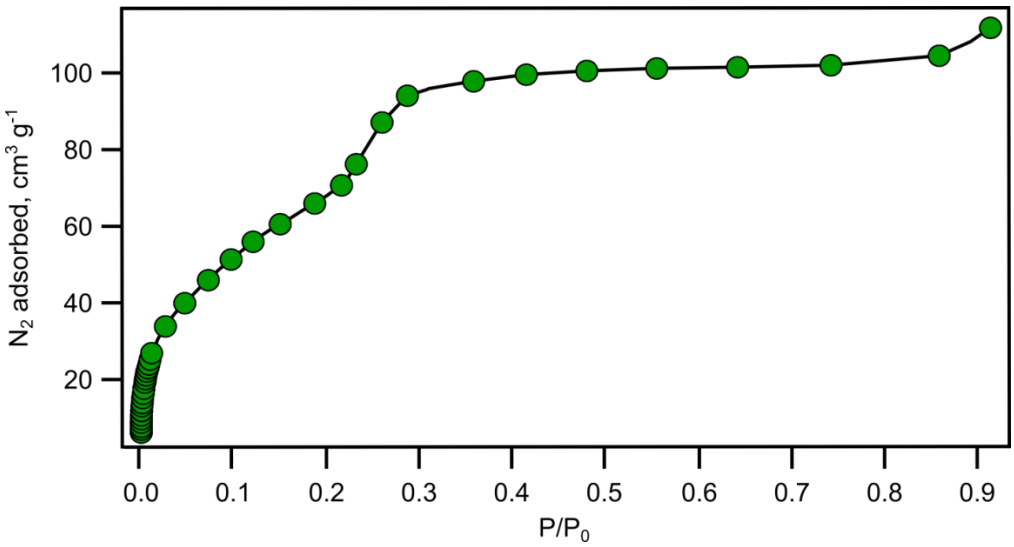

Figure 1.21. N_2 adsorption isotherm of NEM-C_{60}**[1≡(34%)]**.

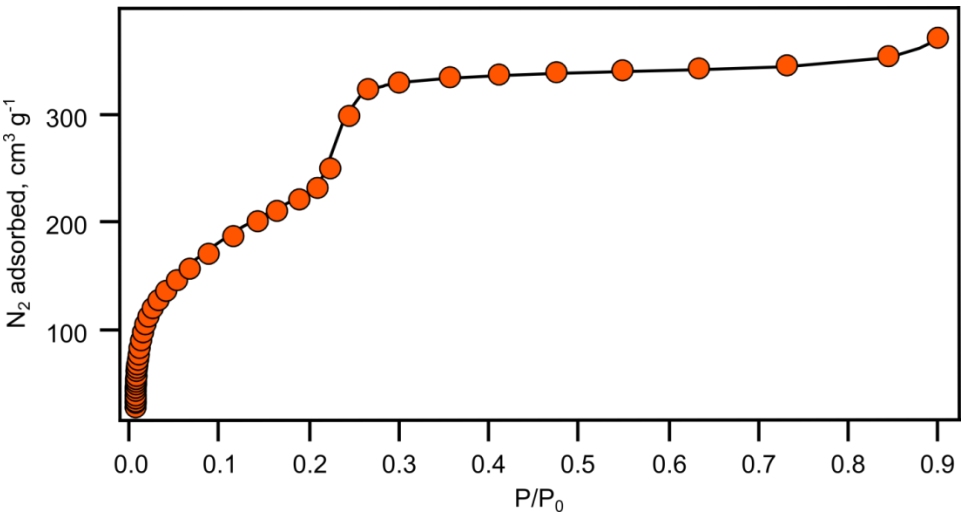

Figure 1.22. N_2 adsorption isotherm of TCNQ**[1≡(50%)]**.

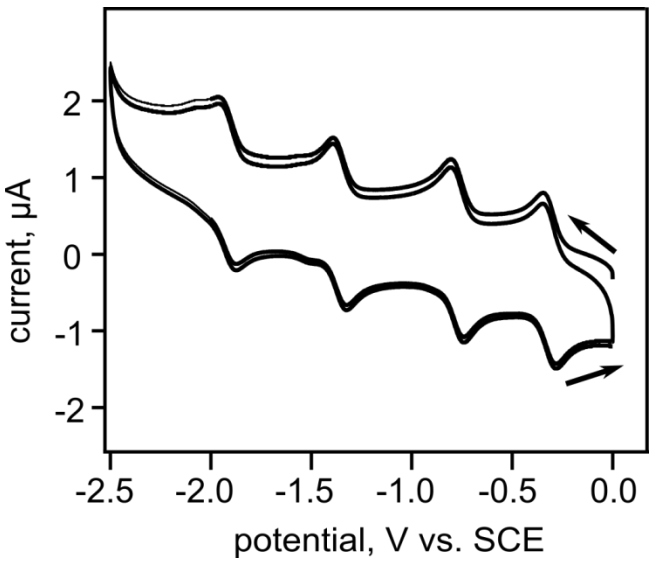

Figure 1.23. Cyclic voltammogram of C_{60} with 0.1 M tetrabutylammonium hexafluorophosphate and 0.5 mM analyte in DMF with a scan rate of 0.1 V. Measurements were performed in a glass solution reservoir equipped with a saturated calomel reference, platinum wire counter, and a glassy carbon working electrode.

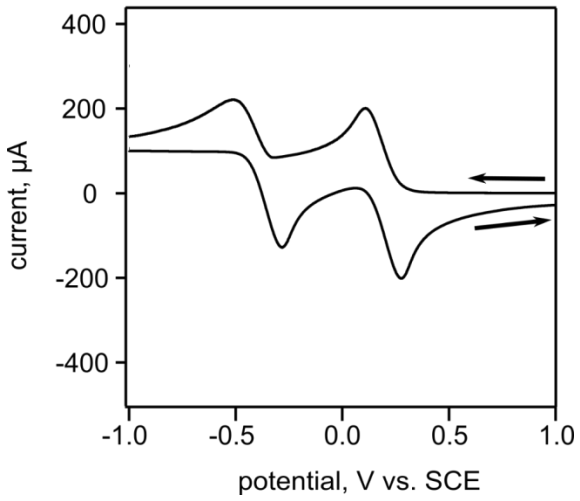

Figure 1.24. Cyclic voltammogram of TCNQ with 0.1 M tetrabutylammonium hexafluorophosphate and 0.5 mM analyte in ACN with a scan rate of 0.1 V. Measurements were performed in a glass solution reservoir equipped with a saturated calomel reference, platinum wire counter, and a glassy carbon working electrode.

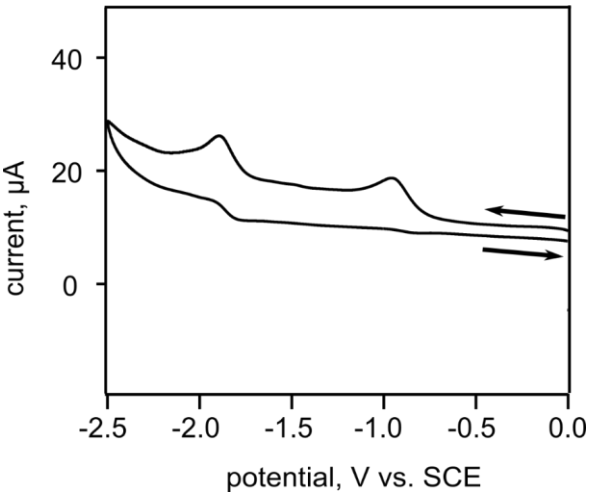

Figure 1.25. Cyclic voltammogram of NEM-C_{60} with 0.1 M tetrabutylammonium hexafluorophosphate and 0.5 mM analyte in DMF with a scan rate of 0.1 V. Measurements were performed in a glass solution reservoir equipped with a saturated calomel reference, platinum wire counter, and a glassy carbon working electrode.

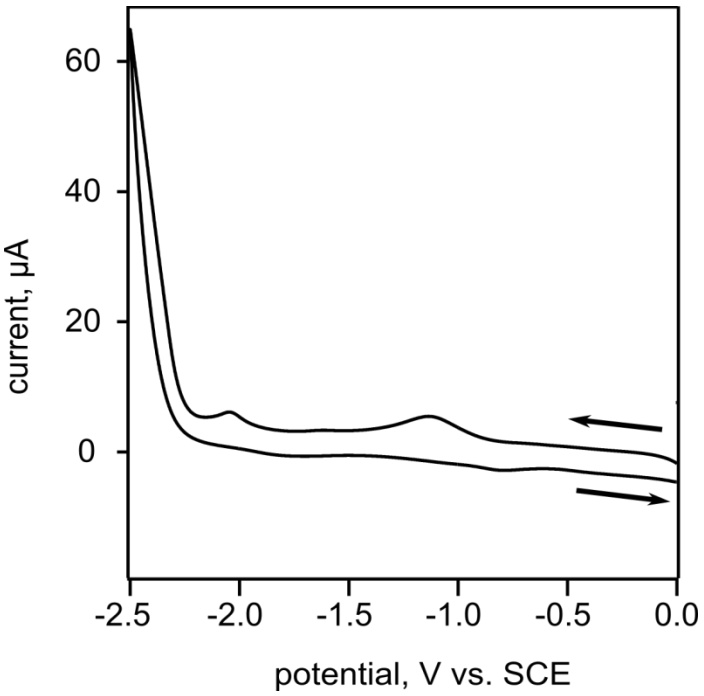

Figure 1.26. Cyclic voltammogram of NEM-C_{60}[**1≡(34%)**] with 0.1 M tetrabutylammonium hexafluorophosphate in DMF with a scan rate of 0.1 V. Measurements were performed in a glass solution reservoir equipped with a saturated calomel reference, platinum wire counter, and a modified glassy carbon working electrode. The gold working electrode was modified with a COF slurry prepared by grinding NEM-C_{60}[**1≡(34%)**] (40 wt.%) and carbon black (60 wt.%) with 0.1 mL of Nafion. The slurry was then pipetted onto the tip of the electrode and dried overnight under high vacuum before use.

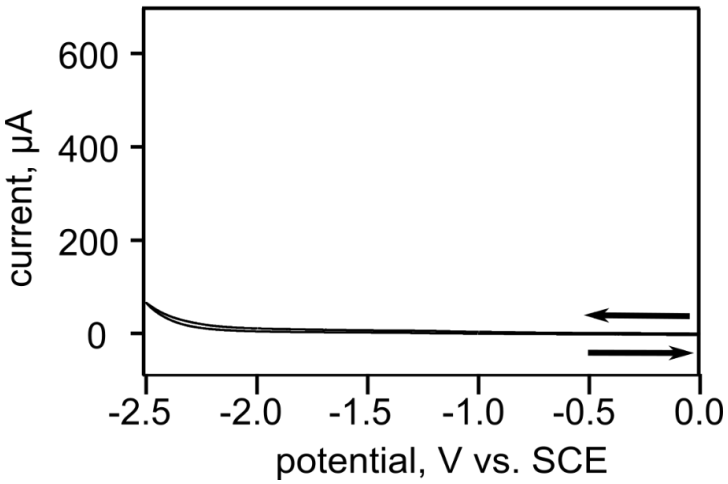

Figure 1.27. Cyclic voltammogram of [**1≡(34%)**] and carbon black as a control with 0.1 M tetrabutylammonium hexafluorophosphate in DMF with a scan rate of 0.1 V. Measurements were performed in a glass solution reservoir equipped with a saturated calomel reference, platinum wire counter, and a modified gold working electrode. The gold working electrode was modified with a COF slurry prepared by grinding **1≡(34%)** (40 wt.%) and carbon black (60 wt.%) with 0.1 mL of Nafion. The slurry was then pipetted onto the tip of the electrode and dried overnight under high vacuum before use.

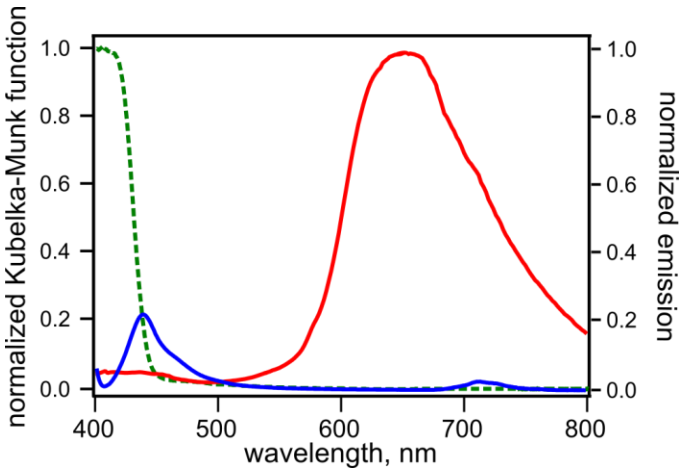

Figure 1.28. Normalized diffuse reflectance (---) and emission (–) spectra of 2-bromoanthracene and emission spectrum (–) of anthracene[**1≡(50%)**] (λ_{ex}= 365 nm) in the solid state.

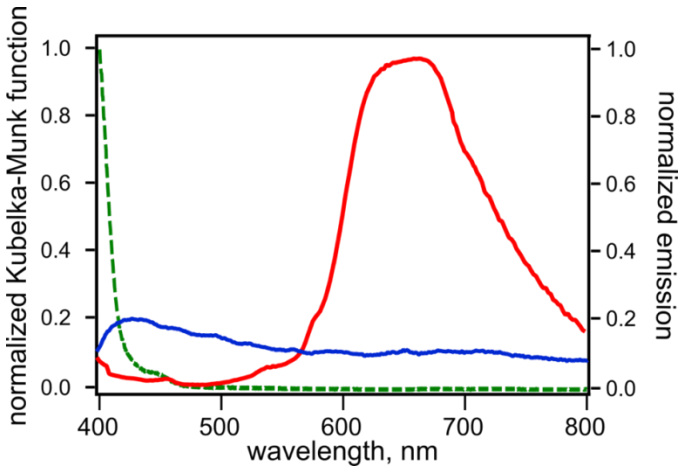

Figure 1.29. Normalized diffuse reflectance (---) and emission (–) spectra of 6-bromo-3-cyano-4-methylcoumarin, and normalized emission spectrum (–) of 4-methyl-2-oxo-2*H*-chromene-3-carbonitrile[**1≡(50%)**] (λ_{ex}= 365 nm) in the solid state.

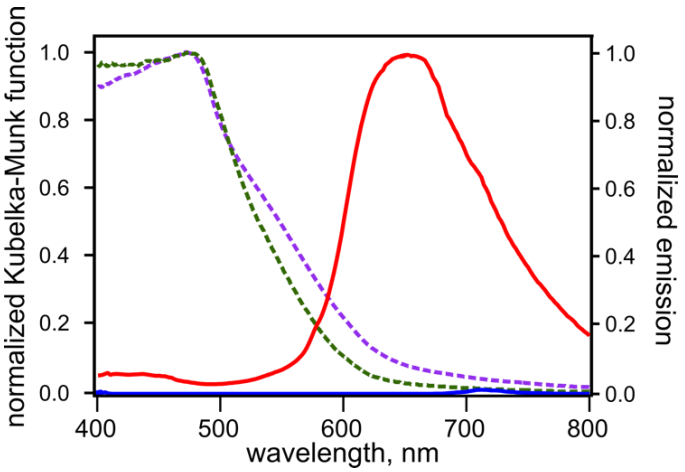

Figure 1.30. Normalized diffuse reflectance (---) and emission (–) spectra of 2-bromoanthracene@TCNQ[**1≡(50%)**], and normalized diffuse reflectance (---) and emission spectra (–) of anthracene[**1≡(50%)**] (λ_{ex}= 365 nm) in the solid state.

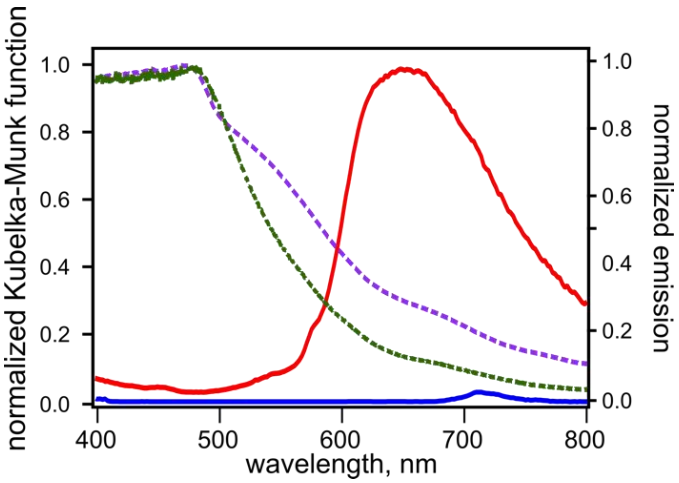

Figure 1.31. Normalized diffuse reflectance (---) and emission (–) spectra of 6-methyl-3-cyano-4-methylcoumarin@TCNQ[**1≡(50%)**] and normalized diffuse reflectance (---), and emission spectra (–) of 4-methyl-2-oxo-2*H*-chromene-3-carbonitrile[**1≡(50%)**] (λ_{ex}= 365 nm) in the solid state.

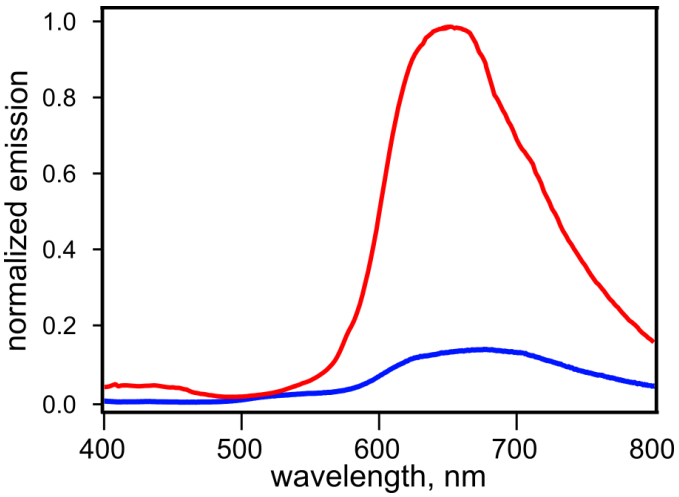

Figure 1.32. Normalized emission spectra of anthracene[**1≡(50%)**] (–) and [**1≡(50%)**] (–) (λ_{ex}= 365 nm) in the solid state.

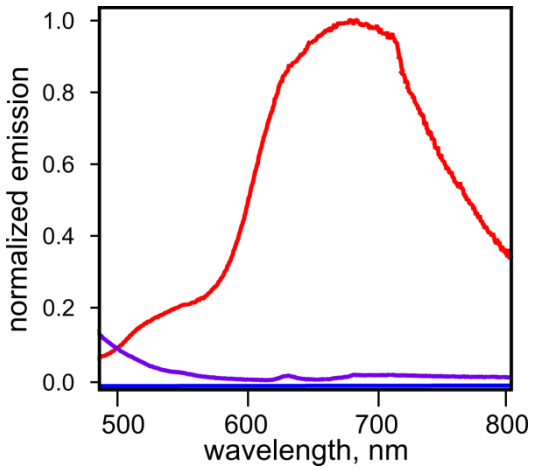

Figure 1.33. Emission spectra of [**1≡(50%)**] (–), TCNQ[**1≡(50%)**] (–), and NEM-C_{60}[**1≡(34%)**](–) (λ_{ex}= 365 nm) in the solid state.

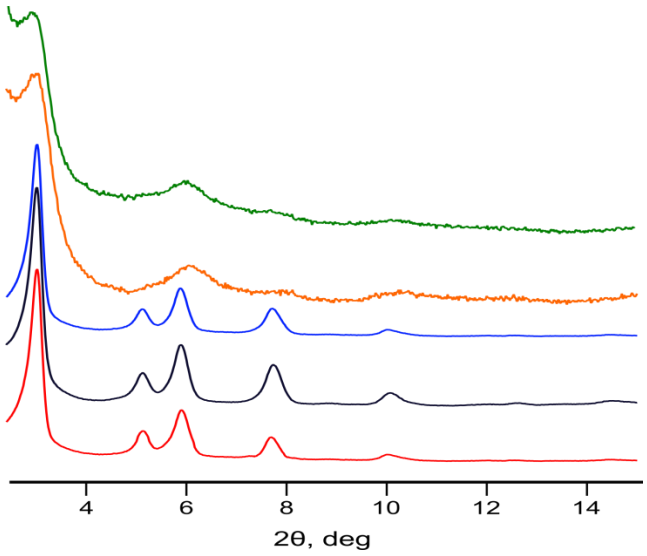

Figure 1.34. PXRD patterns of: 4-methyl-2-oxo-2*H*-chromene-3-carbonitrile[**1≡(50%)**] (green), anthracene[**1≡(50%)**] (orange), 2-bromoanthracene@TCNQ[**1≡(50%)**] (blue), 6-methyl-3-cyano-4-methylcoumarin@TCNQ[**1≡(50%)**] (black), and TCNQ[**1≡(50%)**] (red).

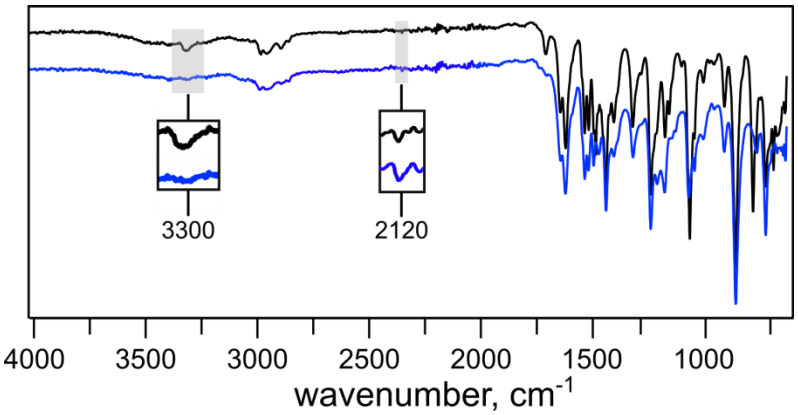

Figure 1.35. FTIR spectra of [**1≡(50%)**] (black) and anthracene[**1≡(50%)**] (blue). The grey areas highlight the disappearance of the H–C≡C (3300 cm^{-1}) and the preservation of the C≡C (2120 cm^{-1}) stretches in anthracene[**1≡(50%)**].

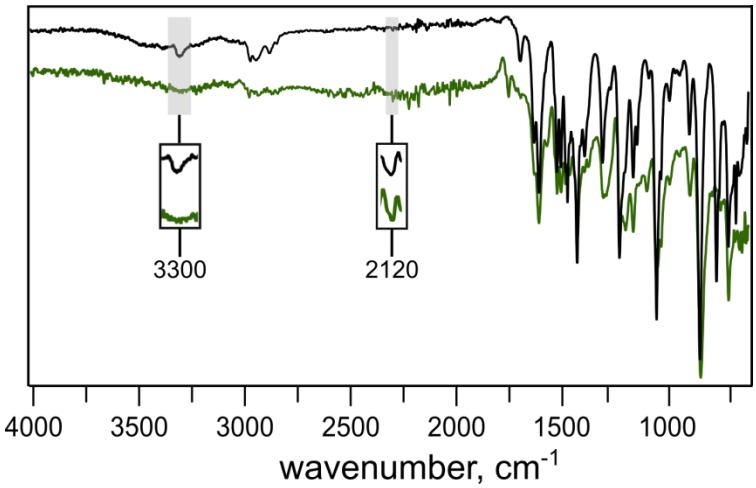

Figure 1.36. FTIR spectra of [**1≡(50%)**] (black) and 4-methyl-2-oxo-2*H*-chromene-3-carbonitrile [**1≡(50%)**] (green). The grey areas highlight the disappearance of the H–C≡C (3300 cm^{-1}) and the preservation of the C≡C (2120 cm^{-1}) stretches in 4-methyl-2-oxo-2*H*-chromene-3-carbonitrile [**1≡(50%)**].

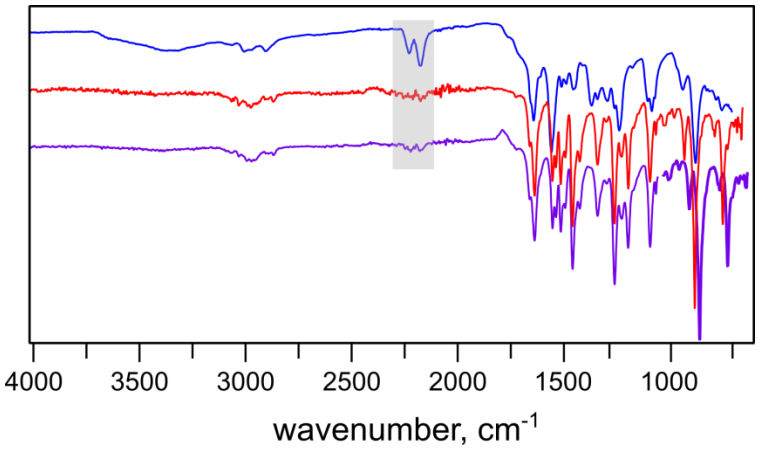

Figure 1.37. FTIR spectra of TCNQ[**1≡(50%)**] (blue), 6-bromo-3-cyano-4-methylcoumarin@TCNQ[**1≡(50%)**] (red), and 2-bromoanthracene@TCNQ[**1≡(50%)**] (purple). The grey area highlights the preservation of the C≡N (2150 cm^{-1}) stretch in all spectra.

REFERENCES

1) M. Matsumoto, R. R. Dasari, W. Ji, C. H. Feriante, T. C. Parker, S. R. Marder, W. R. Dichtel, *J Am Chem Soc* **2017**, *139*, 4999–5002.

2) C. R. Deblase, W. R. Dichtel, *Macromolecules* **2016**, *49*, 5297–5305.

3) A. J. Howarth, C. T. Buru, Y. Liu, A. M. Ploskonka, K. J. Hartlieb, M. McEntee, J. J. Mahle, J. H. Buchanan, E. M. Durke, S. S. Al-Juaid, et al., *Chem. - A Eur. J.* **2017**, *23*, 214–218.

4) L. Zou, X. Yang, S. Yuan, H. -. Zhou, *CrystEngComm* **2017**, *19*, 4868–4871.

5) A. Schneemann, V. Bon, I. Schwedler, I. Senkovska, S. Kaskel, R. A. Fischer, *Chem. Soc. Rev.* **2014**, 6062–6096.

6) O. V Boltalina, A. A. Popov, I. V Kuvychko, N. B. Shustova, S. H. Strauss, *Chem. Rev.* **2015**, *115*, 1051−1105.

7) S. Baudron, *CrystEngComm* **2016**, *18*, 4671–4680.

8) P. J. Waller, F. Gándara, O. M. Yaghi, *Acc. Chem. Res.* **2015**, *48*, 3053–3063.

9) D. A. Vazquez-Molina, G. S. Mohammad-Pour, C. Lee, M. W. Logan, X. Duan, J. K. Harper, F. J. Uribe-Romo, *J. Am. Chem. Soc.* **2016**, *138*, 9767–9770.

10) D. E. Williams, E. A. Dolgopolova, D. C. Godfrey, E. D. Ermolaeva, P. J. Pellechia, A. B. Greytak, M. D. Smith, S. M. Avdoshenko, A. A. Popov, N. B. Shustova, *Angew. Chemie - Int. Ed.* **2016**, *55*, 9070–9074.

11) J. Sukegawa, C. Schubert, X. Zhu, H. Tsuji, D. M. Guldi, E. Nakamura, *Nat. Chem.* **2014**, *6*, 899–905.

12) C.-Z. Li, H.-L. Yip, A. K.-Y. Jen, *J. Mater. Chem.* **2012**, *22*, 4161–4177.

13) H. Yang, S. Zhang, L. Han, Z. Zhang, Z. Xue, J. Gao, Y. Li, C. Huang, Y. Yi, H. Liu, et al., *ACS Appl. Mater. Interfaces* **2016**, *8*, 5366–5375.

14) H. S. Sasmal, H. B. Aiyappa, S. N. Bhange, S. Karak, A. Halder, S. Kurungot, R. Banerjee, *Angew. Chem. Int. Ed.* **2018**, *57*, 10894–10898.

15) S. Cai, Y. Zhang, A. B. Pun, B. He, J. Yang, F. M. Toma, I. D. Sharp, O. M. Yaghi, J. Fan, S. Zheng, *Chem. Sci.* **2014**, *5*, 4693–4700.

16) S. Duhovic, M. Dinca, *Chem. Mater.* **2015**, *27*, 5487–5490.

17) H. Guo, J. Wang, Q. Fang, Y. Zhao, S. Gu, J. Zheng, Y. Yan, *CrystEngComm* **2017**, *19*, 4905–4910.

18) D. A. Vazquez-Molina, G. S. Mohammad-Pour, C. Lee, M. W. Logan, X. Duan, J. K. Harper, F. J. Uribe-Romo, *J Am Chem Soc* **2016**, *138*, 9767–9770.

19) E. Jin, M. Asada, Q. Xu, S. Dalapati, M. A. Addicoat, M. A. Brady, H. Xu, T. Nakamura, T. Heine, Q. Chen, et al., *Science (80-.).* **2017**, *676*, 673–676.

20) X. Feng, X. Ding, D. Jiang, *Chem. Soc. Rev.* **2012**, *41*, 6010–6022.

21) M. S. Lohse, T. Bein, *Adv. Funct. Mater.* **2018**, *28*, 1705553.

22) R. P. Bisbey, W. R. Dichtel, *ACS Cent. Sci.* **2017**, *3*, 533–543.

23) C. D. Wessendorf, R. Eigler, S. Eigler, J. Hanisch, A. Hirsch, E. Ahlswede, *Sol. Energy Mater. Sol. Cells* **2015**, *132*, 450–454.

24) A. Hirsch, *The Chemistry of Fullerenes*, John Wiley And Sons, Inc., **2008**.

25) D. M. Guldi, *Chem. Commun.* **2000**, 321–327.

26) D. Josa, E. M. Cabaleiro-lago, L. A. Santos, T. C. Ramalho, *J. Phys. Chem. C* **2014**, *118*, 9521−95289522.

27) A. M. Rice, E. A. Dolgopolova, B. J. Yarbrough, G. A. Leith, C. R. Martin, K. S. Stephenson, R. A. Heugh, A. J. Brandt, D. A. Chen, S. G. Karakalos, et al., *Angew. Chemie Int. Ed.* **2018**, *57*, 11310–11315.

28) S. Goswami, D. Ray, K. Otake, C. Kung, S. J. Garibay, T. Islamoglu, A. Atilgan, Y. Cui, C. J. Cramer, O. K. Farha, et al., *Chem. sc* **2018**, *9*, 4477–4482.

29) A. A. Talin, A. Centrone, A. C. Ford, M. E. Foster, V. Stavila, P. Haney, R. A. Kinney, V. Szalai, F. El Gabaly, H. P. Yoon, et al., *Science (80-.).* **2014**, *343*, 66–70.

30) L. Chen, K. Furukawa, J. Gao, A. Nagai, T. Nakamura, D. Yuping, D. Jiang, *J Am Chem Soc* **2014**, *136*, 9806–9809.

31) D. D. Medina, V. Werner, F. Auras, R. Tautz, M. Dogru, S. Linke, M. Do, J. Feldmann, P. Knochel, T. Bein, *ACS Nano* **2014**, *8*, 4042–4052.

32) M. Dogru, M. Handloser, F. Auras, T. Kunz, D. Medina, A. Hartschuh, P. Knochel, T. Bein, *Angew. Chem. Int. Ed.* **2013**, *52*, 2920–2924.

33) J. Guo, Y. Xu, S. Jin, L. Chen, T. Kaji, Y. Honsho, M. A. Addicoat, J. Kim, A. Saeki, H. Ihee, et al., *Nat. Commun.* **2013**, *4*, 2736.

34) M. Kivala, C. Boudon, J. Gisselbrecht, P. Seiler, M. Gross, F. Diederich, *Chem. Commun.* **2007**, 4731–4733.

35) H. Xu, J. Gao, D. Jiang, *Nat. Chem.* **2015**, *7*, 905–912.

36) R. Chinchilla, C. Najera, *Chem Soc Rev* **2011**, *40*, 5084–5121.

37) A. M. Rice, E. A. Dolgopolova, N. B. Shustova, *Chem. Mater.* **2017**, *29*, 7054–7061.

38) P. Hu, K. Du, F. Wei, H. Jiang, C. Kloc, *Cryst. Growth Des.* **2016**, *16*, 3019−3027.

39) K. Kanai, K. Akaike, K. Koyasu, K. Sakai, T. Nishi, Y. Kamizuru, *Appl. Phys. A* **2009**, *95*, 309–313.

40) H. Alves, R. M. Pinto, E. S. MaçÔas, *Nat. Commun.* **2013**, *4*, 1842.

41) F. D'Souza, O. Ito, *Coord. Chem. Rev.* **2005**, *249*, 1410–1422.

42) C. R. DeBlase, K. E. Silberstein, T.-T. Truong, H. D. Abruña, W. R. Dichtel, *J. Am. Chem. Soc.* **2013**, *135*, 16821–4.

43) T. Rajendran, B. Manimaran, R.-T. Liao, Y.-H. Liu, P. Thanasekaran, R.-J. Lin, I.-J. Chang, P.-T. Chou, R. Ramaraj, S. Rajagopal, et al., *Dalt. Trans.* **2010**, *39*, 2928–2935.

44) A. Sastre-Santos, C. Parejo, L. Martin-Gomis, K. Ohkubo, F. Fernandex-Lazaro, S. Fukuzumi, *J. Mater. Chem.* **2011**, *21*, 1509–1515.

45) J. I. Kadokawa, Y. Tanaka, Y. Yamashita, K. Yamamoto, *Eur. Polym. J.* **2012**, *48*, 549-559.

46) S. Jeon, S. Park, J. Nam, Y. Kang, J. M. Kim, *ACS Appl. Mater. Interfaces* **2016**, *8*, 1813–1818.

47) M. G. Schwab, M. Hamburger, X. Feng, J. Shu, H. W. Spiess, X. Wang, M. Antonietti, K. Müllen, *Chem. Commun.* **2010**, *46*, 8932–8934.

48) H. Xu, J. Gao, D. Jiang, *Nat. Chem.* **2015**, *7*, 905–912.

49) J.-C. Wu, D.-X. Wang, Z.-T. Huang, and M.-X. Wang, *J. Org. Chem.* **2010**, *75*, 8604–8614

50) M. Kivala, C. Boudon, J.-P. Gisselbrecht, P. Seiler, M. Griss, and F. Diederich, *Chem. Commun.*, **2007**, 4731–4733

51) R. Chinchilla, and C. Najera, *Chem. Soc. Rev.*, **2011**, *40*, 5084–5121.

52) S. Sasaki, K. Igawa, and G.I. Konishi. *J. Mater. Chem. C.*, **2015**, *3*, 5940–5950.

53) Y. Mizobe, M. Miyata, I. Hisaki, Y. Hasegawa, N. Tohnai, *Org. Lett.* **2006**, *8*, 4295–4298.

54) Y. Sun, Y. Sun, S. Zhao, D. Cao, R. Guan, Z. Liu, X. Yu, X. Zhao, *Asian J. Org. Chem.* **2018**, *7*, 197–202.

55) R. Cui, Y. Lv, Y. Zhao, N. Zhao, N. Li, *Mater. Chem. Front.*, **2018**, *2*, 910-916.

56) K. W. Chapman, D. F. Sava, G. J. Halder, P. J. Chupas, T. M. Nenoff, *J. Am. Chem. Soc.*, **2011**, *133*, 18583–18585.

57) **APEX3** Version 2016.5-0 and **SAINT+** Version 8.37A. Bruker AXS, Inc., Madison, Wisconsin, USA, 2016.

58) L. Krause, R. Herbst-Irmer, G. M. Sheldrick, D. Stalke, *J. Appl. Cryst.* **2015**, *48*, 3-10.

59) G. M. Sheldrick, *Acta Cryst.* **2015**, *A71*, 3–8

60) G. M. Sheldrick, *Acta Cryst.* **2015**, *C71*, 3–8

61) O. V. Dolomanov, L. J. Bourhis, R. J. Gildea, J. A. K. Howard, H. Puschmann, *J. Appl. Cryst*. **2009**, *42*, 339–341.

62) A. Sarkar, L. Evans, and M. Stefik, *Langmuir*, **2018**, *34*, 5738–5749.

63) A.S. Duke, E.A. Dolgopolova, R.P. Galhenage, S.C. Ammal, A. Heyden, M.D. Smith, D.A. Chen, N.B. Shustova, *J. Phys. Chem. C*. **2015**, *119*, 27457–27466.

64) E.A. Dolgopolova, A.J. Brandt, O.A. Ejegbavwo, A.S. Duke, T.D. Maddumapatabandi, R.P. Galhenage, B.W. Larson, O.G. Reid, S.C. Ammal, A. Heyden, M. Chandrashekhar, V. Stavila, D.A. Chen, N.B. Shustova, *J. Am. Chem. Soc*. **2017**, 139, 5201–5209.